THE EVOLUTION OF LAVES PHASE PRECIPITATION IN AISI 441 UNDER SOFC OPERATING CONDITIONSAND THE EFFECTS ON OXIDE GROWTH

by

Christopher Isadore Zimny

A thesis submitted in partial fulfillment
of the requirements for the degree

of

Master of Science

in

Mechanical Engineering

MONTANA STATE UNIVERSITY

Bozeman, Montana

January 2016

©COPYRIGHT

by

Christopher Isadore Zimny

2016

All Rights Reserved

ACKNOWLEDGEMENTS

First I would like to express my sincere gratitude towards my mentoring professor and committee chair, Dr. Roberta Amendola, for granting me the opportunity to pursue interesting materials science research while providing continuous encouragement and support throughout the duration of the project, especially as I finished this thesis remotely. Additionally, I thank my committee members, Dr. Paul Gannon and Dr. Stephen Sofie, for their insightful comments and discussions that refined this research into its final form. I deeply appreciate the time and effort these three individuals devoted to the completion of this research and thesis paper.

Many others contributed their resources to the research that accumulated in this paper as well. In particular, I would like to thank Alleghany Ludlum and National Kwikmetal Service for providing the samples that were tested. Additional thanks goes to the staff of the Imaging and Chemical Analysis Laboratory (ICAL) at Montana State University, Bozeman for their assistance with analysis. I am also grateful towards my fellow student researches who worked along with me on this project, including John Ryter and Chaparral Berry.

Lastly, the love and support of my friends and family were indispensable in the completion of this study. Thank you all for standing by me throughout this process as this Master's thesis would never have been completed without you.

TABLE OF CONTENTS

1. INTRODUCTION 1

Fossil Fuels in Energy Infrastructure 1
Overview of Fuel Cell Operation 2

2. BACKGROUND 6

Solid Oxide Fuel Cell Operation Overview 6
Interconnect Materials 7
Requirements of the Interconnect 7
Evolution of Interconnect Materials 8
Metallic Interconnect Materials 9
FSS ICs 10
Previous Metallic Interconnect Corrosion Research 11
Single and Dual Atmosphere Effects on FSS Oxidation 11
Selection of Ferritic Stainless Steel AISI 441 13
Impact of Moisture on TGO 15
Ferritic Stainless Steel Microstructural Evolution 17
Historical Laves Phase Research of FSS 19

3. EXPERIMENTAL PROCEDURE 21

Sample Preparation and Definition 21
Single Atmosphere Experimental Procedure 22
Dual Atmosphere Experimental Procedure 22
Vacuum Experimental Procedure 24
Metallographic Sample Preparation 25
Analytic Techniques 26
FE-SEM 26
Scanning Electron Microscope 27
ImageJ Analysis Technique 28

4. RESULTS AND DISCUSSION 32

The Initial Detection Precipitates 32
Electron Backscatter Diffraction 32
Microstructural Analysis 34
As-Received Samples 34
Single Atmosphere Exposure 36
Dual Atmosphere Exposure 37

TABLE OF CONTENTS – CONTINUED

Vacuum Furnace Heat Treatment 40
Surface Oxide Evolution 41
As-Received Protective Chromium Oxide 41
Single Atmosphere Exposure Oxide Evolution 45
Dual Atmosphere Exposure Oxide Evolution 55
Vacuum Furnace Heat Treatment Oxide Evolution 66
Progression of Oxide Scale Growth Over Time 66
Comparison of Oxide Evolution after Environment Exposure 69
Effects of Thickness and Grain Size on Oxidation 70
Laves Phase Evolution 72
Single Atmosphere Laves Phase Evolution 72
Dual Atmosphere Laves Phase Evolution 75
Progression of Laves Phase Density Over Time 76
Comparison of Laves Phase Evolution across Environment Types 77

5. CONCLUSION 81

Summary of Study 81
Future Work 83

REFERENCES 85

LIST OF FIGURES

Figure Page

1.2.1: Operating Mechanism of Oxygen-Ion-Conducting Fuel Cell 2

1.2.2: Operating Mechanism of Proton-Conducting Fuel Cell 3

1.2.3: Operating principle of a fuel cell 4

1.2.4: Schematic of Planar Fuel Cell Stack 5

2.1.1: Schematic of SA and DA exposures (8) 7

2.4.1: SEM surface images for AISI 430 exposed to 200 hr 800°C single (a) and dual (b) atmospheres 14

2.4.2: SEM surface images of FSS 441 with inset selected area electron diffraction (Kikuchi) patterns for single (a) and dual (b) atmosphere exposures 14

2.4.3: SEM cross-section images with EDS line scans of FSS 441 after 200 hr, 800°C single (a) and dual (b) atmosphere exposures – different magnifications. (20) 15

2.4.4: Proposed mechanism for the oxidation of Fe-Cr alloys in water vapor at high temperatures (24) 16

2.4.5: Unit Cell of Body Centered Cubic Crystalline Structure (26). 17

2.4.6: AB_2 Laves Phase Structure C15. The large symbols are the A component and the small symbols are the B component. The broken lines and shaded symbols indicate one primitive cell. (29) 18

2.4.7: The Laves Phase Volume Fraction – Temperature/Time Curves during Isothermal Annealing of AISI 441 in SA (27) 19

3.3.1: Dual atmosphere coupon mount 23

3.3.2: Assembled dual atmosphere testing apparatus 23

LIST OF FIGURES - CONTINUED

Figure Page

3.5.1: Epoxy Sandwich Mounting Method for Sample Preparation (34) 25

3.6.1: Zeiss Spura 55VP Field Emission Scanning Electron Microscope 27

3.6.2: JEOL JSM-6100 Scanning Electron Microscope 28

3.6.3: Image before and after ImageJ Manipulation for Isolating Nodules 29

3.6.4: 1.2mm SA cross-section with large geometries: a) slope between grains, b) general roughness after etching. 30

4.1.1: FE-SEM microstructure images taken of 0.5 mm thick AISI 441 samples after etching a) as-received and b) dual-atmosphere specimens 33

4.1.2: Electron Back Scatter Diffraction Image to Detect Laves Phase 34

4.2.1: As-received samples of thickness a) 0.5 mm and b) 1.2 mm 36

4.2.2: Single atmosphere exposure for 100 hours on thicknesses a) 0.5 mm and b) 1.2 mm 37

4.2.3: Dual atmosphere exposure for 100 hours on thicknesses a) 0.5 mm and b) 1.2 mm 38

4.2.4: Energy dispersive x-ray spectroscopy scan locations of FSS 441 cross-section at a) grain boundary precipitate, b) intra-grain precipitate, and c) large nodule 39

4.2.5: Samples exposed to 800°C in a vacuum furnace for 100 hours on thicknesses a) 0.5 mm and b) 1.2 mm 40

4.3.1: As-received AISI 441 oxide layer on 0.5 mm thick before exposure accompanied by EDX line scan composition. 42

LIST OF FIGURES - CONTINUED

Figure Page

4.3.2 As-received AISI 441 oxide layer on 1.2 mm thick before exposure accompanied by EDX line scan composition. 43

4.3.3: Surface oxides of as-received samples. a) 0.5 and b) 1.2 mm samples. 44

4.3.4 Surface Oxide Composition of 0.5 mm Control Sample 44

4.3.5: Surface Oxide Composition of 1.2 mm Control Sample 45

4.3.6: Development of AISI 441 oxide layer on 0.5 mm thick sample at 24 hours under single atmosphere exposure accompanied by EDX line scan composition. 47

4.3.7: Development of AISI 441 oxide layer on 0.5 mm thick sample at 48 hours under single atmosphere exposure accompanied by EDX line scan composition. 48

4.3.8: Development of AISI 441 oxide layer on 0.5 mm thick sample at 72 hours under single atmosphere exposure accompanied by EDX line scan composition. 49

4.3.9: Development of AISI 441 oxide layer on 0.5 mm thick sample at 100 hours under single atmosphere exposure accompanied by EDX line scan composition. 50

4.3.10: Development of AISI 441 oxide layer on 1.2 mm thick sample at 24 hours under single atmosphere exposure accompanied by EDX line scan composition. 51

4.3.11: Development of AISI 441 oxide layer on 1.2 mm thick sample at 48 hours under single atmosphere exposure accompanied by EDX line scan composition. 52

4.3.12: Development of AISI 441 oxide layer on 1.2 mm thick sample at 72 hours under single atmosphere exposure accompanied by EDX line scan composition. 53

LIST OF FIGURES - CONTINUED

Figure Page

4.3.13: Development of AISI 441 oxide layer on 1.2 mm thick sample at 100 hours under single atmosphere exposure accompanied by EDX line scan composition. 54

4.3.14: EDX spot scan of inner oxide on DA sample 56

4.3.15: EDX spot scan of outer oxide on DA sample 57

4.3.16: Development of AISI 441 oxide layer on 0.5 mm thick sample at 24 hours under dual atmosphere exposure accompanied by EDX line scan composition. 58

4.3.17: Development of AISI 441 oxide layer on 0.5 mm thick sample at 48 hours under dual atmosphere exposure accompanied by EDX line scan composition. 59

4.3.18: Development of AISI 441 oxide layer on 0.5 mm thick sample at 72 hours under dual atmosphere exposure accompanied by EDX line scan composition. 60

4.3.19: Development of AISI 441 oxide layer on 0.5 mm thick sample at 100 hours under dual atmosphere exposure accompanied by EDX line scan composition. 61

4.3.20: Development of AISI 441 oxide layer on 1.2 mm thick sample at 24 hours under dual atmosphere exposure accompanied by EDX line scan composition. 62

4.3.21: Development of AISI 441 oxide layer on 1.2 mm thick sample at 48 hours under dual atmosphere exposure accompanied by EDX line scan composition. 63

4.3.22: Development of AISI 441 oxide layer on 1.2 mm thick sample at 72 hours under dual atmosphere exposure accompanied by EDX line scan composition. 64

LIST OF FIGURES - CONTINUED

Figure Page

4.3.23: Development of AISI 441 oxide layer on 1.2 mm thick sample at 100 hours under dual atmosphere exposure accompanied by EDX line scan composition. 65

4.3.24: Oxide growth of 0.5 mm thick samples after exposure to specified times of single and dual atmosphere testing at 800°C. 68

4.3.25: Oxide growth of 1.2 mm thick samples after exposure to specified times of single and dual atmosphere testing at 800°C. 68

4.3.26: Oxide Thickness after 100 Hours of Exposure at 800°C to the Specified Atmosphere. 70

4.4.1: Location of measurements for evaluation of Laves phase precipitation where A) corresponds to Edge 1 (Hydrogen-side in DA), B) is the Center of the sample, and C) is Edge 2 (Oxygen-side in DA). 73

4.4.2: Laves phase area percent through cross-section of 1.2 mm thick samples exposed to single atmosphere over different time intervals shown with 95% confidence intervals. 73

4.4.3: Laves phase area percent through cross-section of a) 0.5 and b) 1.2mm thick samples exposed to single atmosphere over different time intervals. 75

4.4.4: Laves phase area percent through cross-section of a) 0.5 and b) 1.2mm thick samples exposed to dual atmosphere over different time intervals. 76

4.4.5: Average Laves phase area percent of 0.5mm and 1.2mm thick samples exposed to single and dual atmospheres at specific time intervals. 77

4.4.6: Laves phase area percent through cross-section of a) 0.5 and b) 1.2 mm thick samples exposed to various atmospheres for 100 hours. 79

LIST OF FIGURES - CONTINUED

Figure Page

4.4.7: Average Laves phase area percent of 0.5mm and 1.2mm thick samples exposed to various atmospheres for 100 hours. 80

LIST OF TABLES

Table Page

3.1.1: Batch Composition for AISI 441 FSS Alloys as Stated by Manufacturer 21

3.5.1: Metallographic Polishing Procedure (36) 26

4.2.1: Qualitative Elemental Composition of Features for AISI 441 FSS Alloys 39

4.3.1: Evolution of Cross-Sectional Oxide Thickness in SA Exposure over Time. 46

4.3.2: Evolution of Cross-Sectional Oxide Thickness in SA Exposure over Time. 55

4.3.3: Cross-Sectional Oxide Thickness after Vacuum Furnace Testing. 66

ABSTRACT

Recent research on solid oxide fuel cell technologies – a type of high temperature fuel cell – has resulted in the reduction of operating temperatures from around 1000°C to an intermediate range of 600-800°C. This reduction in temperature allows previously unviable materials to be investigated for use with this system. Interconnects, the component that separates the anode and cathode of adjacent fuel cells, benefit from this advancement as metals may now be utilized in place of the ceramic interconnects traditionally used in solid oxide fuel cell systems. In separating the anode and cathode, interconnects are necessarily subjected to what is known as dual atmosphere exposure: the exposure to the fuel, H_2, on one side of the material and the oxidant, air, on the other side. These extreme operating conditions have unusual effects on materials.

AISI 441 is one promising ferritic stainless steel alloy for use as an interconnect; however, under dual atmosphere exposure, AISI 441 sees accelerated and anomalous oxide growth, exceeding that of similar ferritic stainless steels. This study investigated the oxide and Laves phase precipitate evolution of AISI 441 subjected to various environments including single, dual, and vacuum environments at a temperature of 800°C. Additionally, the relationship between the precipitates and the oxide formation was observed. Analysis was performed with a variety of equipment including a field emission scanning electron microscope.

In environments containing oxygen, the oxide thickness of AISI 441 was found to increase over time and saw accelerated oxide formation in the dual atmosphere test, corroborating previous research. This study went on to investigate the formation of Laves phase precipitate Fe_2Nbin the microstructure of AISI 441 as a result of atmosphere. Laves phase materials are under research as hydrogen storage materials, suggesting the existence of these phases may facilitate hydrogen transport and storage in materials used as interconnects. Increased hydrogen transport could potentially explain the accelerated and anomalous oxidation of AISI 441 compared to other ferritic stainless steels. Over the time frames tested, the environments had no apparent effect on the Laves phase precipitation; further testing should investigate Laves phase precipitation between 0 and 1000 minutes.

CHAPTER ONE

INTRODUCTION

Fossil Fuels in Energy Infrastructure

Combustion of fossil fuels is the most widely used energy generation process; however, it suffers from many drawbacks, including low efficiencies and high pollution levels (1; 2). In order to mitigate the growing global pollution and meet an increasing energy demand, new attention has been directed towards the development of alternative energy sources. Wind, solar, and nuclear energy have had the eye of the media in recent years and contribute noticeably to the energy supply; however, these energy generation methods are not currently capable of displacing fossil fuels as the major source of electricity. While it is unlikely that we will move away from fossil fuels in the near future, perhaps the method for extracting energy from these sources can be refined.

Multiple energy transformation steps are required to generate electricity from fossil fuels when used in a combustion system. A chemical reaction is used to generate thermal energy which – in turn – drives a machine, often a turbine. The mechanical motion of the machine then interacts with a generator to produce electricity. An alternative method for extracting the chemical energy stored within fuels is a direct conversion to electrical energy with no intermediary steps in devices known as fuel cells. By avoiding the thermal and mechanical components of this reaction, electrical energy generation from chemical fuels becomes more efficient and reduces harmful byproducts.

Overview of Fuel Cell Operation

Fuel cells make use of the electrochemical reaction that occurs when a fuel is directly oxidized without combustion. When hydrogen is used as a fuel and oxygen as the oxidant, this reaction may appear in one of two forms: oxygen-ion-conducting fuel cells and proton-conducting fuel cells. The basic reaction of each can be seen in Figure 1.2.1 and Figure 1.2.2 (3).

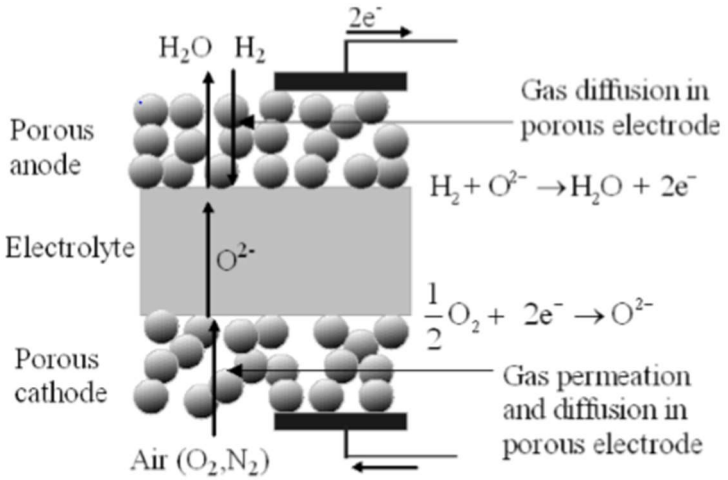

Figure 1.2.1: Operating Mechanism of Oxygen-Ion-Conducting Fuel Cell

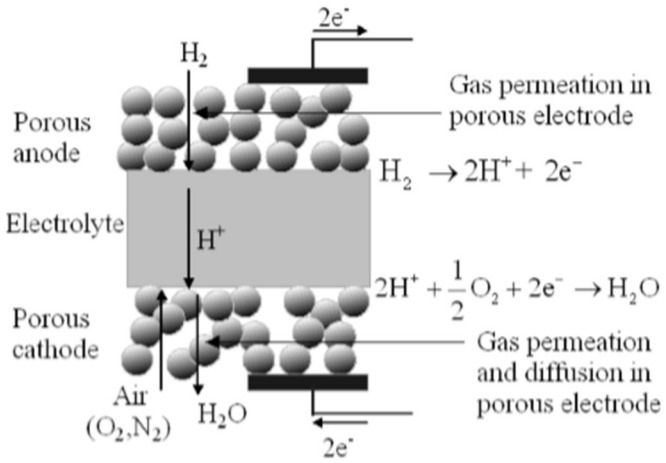

Figure 1.2.2: Operating Mechanism of Proton-Conducting Fuel Cell

With the overall fuel cell chemical reaction being summarized as:

Equation 1: Oxygen-Ion-Conducting Fuel Cell Reaction

$$\frac{1}{2}O_2 + 2e^- \rightarrow O^{2-}$$

$$H_2 + O^{2-} \rightarrow H_2O + 2e^-$$

Equation 2: Proton-Conducting Fuel Cell Reaction

$$H_2 \rightarrow 2H^+ + 2e^-$$

$$2H^+ + \frac{1}{2}O_2 + 2e^- \rightarrow H_2O$$

Some fuel cells require the pure components in order to operate. Other fuel cells, such as solid oxide fuel cells (SOFC), may readily use a variety of fuels including hydrocarbons and alcohols, thereby allowing current fuel supplies to be fully utilized – albeit with less pollution and more energy generated than when used with internal combustion engines.

Various fuel cell systems exist but all rely on the liberation of charged particles, namely ions, protons, and electrons. Three major components are necessary to instigate and sustain the reaction [Figure 1.2.3] (4): the anode that allows the fuel to flow toward

the electrolyte, the cathode that permits the oxidant to diffuse toward the electrolyte, and the electrolyte that serves to conduct ions from either the cathode to the anode or from the anode to the cathode. Only unidirectional flow is allowed through the electrolyte, but different configurations of fuel cells are known to make use of both. Lower temperature fuel cells incorporate a catalyst (often platinum) in the anode to facilitate the reduction of hydrogen into a hydrogen ion and electron, thus permitting the flow of electricity. High temperature fuel cells bypass the need for a catalyst as the high operating temperature provides enough energy to instigate oxidation.

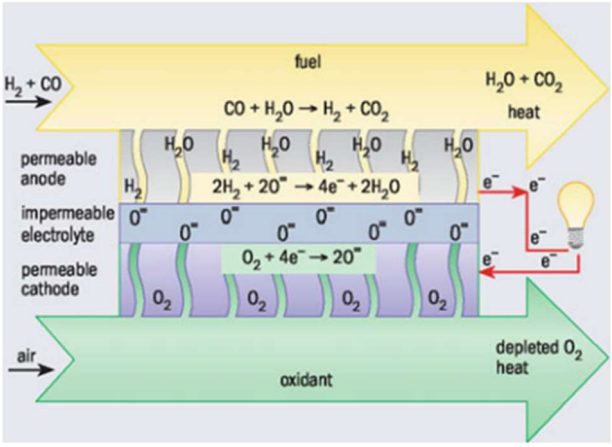

Figure 1.2.3: Operating principle of a fuel cell (4)

Despite the variation that exists among fuel cell types, each individual cell can only generate a small amount of power. To compensate for the low individual cell energy output, fuel cells may be placed in series, similar to batteries, to allow the electricity generated by each to be combined into a more useful quantity. The most common method of placing fuel cells in series is to vertically layer fuel cells in what is known as a planar fuel cell stack. In order to maintain separation of chemical environments in each fuel cell,

a new component, the interconnect (IC), is introduced to the stack. The functions of ICs can be summarized as an electrical connection and physical barrier between the anode and cathode of adjacent cells [Figure 1.2.4] (5). This study will focus on IC compatibility issues as seen in the SOFC operating environment, particularly the evolution of precipitates and oxide layers of ferritic stainless steels.

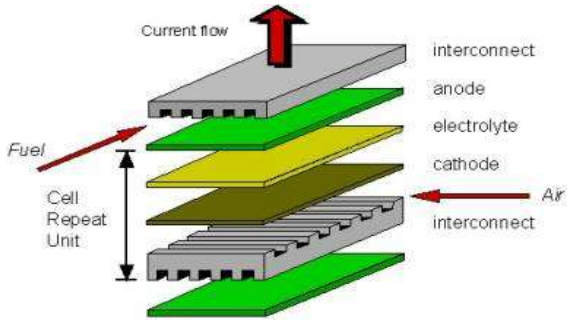

Figure 1.2.4: Schematic of Planar Fuel Cell Stack (6)

CHAPTER TWO

BACKGROUND

Solid Oxide Fuel Cell Operation Overview

SOFCs operate between 600 and 1000°C; an operating temperature range that imposes many restrictions on the design and use of materials. Often ceramics and other solid materials are necessary to meet the requirements of SOFCs. Typical SOFC component materials are as follows: anodes are a nickel and yttria-stabilized zirconia (YSZ) cermet, cathodes are made of a lanthanum-doped manganite, and electrolytes are YSZ. While these are the usual materials, other materials are used in SOFC systems; SOFCs are not as well developed as many other fuel cell technologies, so a great deal of research activity is focused on these systems and materials (7). In stacks, ICs have traditionally been ceramic materials, such as lanthanum chromite. However, lower temperature SOFCs allow metallic interconnects as a possibility.

Interconnects of SOFCs separate the fuel and oxidant sides of adjacent fuel cells in fuel cells stacks, thus exposing ICs to a very reactive environment. This exposure to two, distinct environments is known as dual atmosphere exposure and increases the complexity of IC material selection. An example of samples exposed to single (SA) and dual (DA) atmosphere can be seen below [Figure 2.1.1]. Here the environments are simplified to air and hydrogen. In fuel cells, the oxidizing and reducing environments would likely be more complex as the fuel would break down into additional components. For example if a hydrocarbon is used as the fuel, carbon would be a byproduct in the

system allowing for the formation of CO_2 and carburization to occur within the fuel cell. This has implications beyond the scope of this study. To focus on the desired issues, the simple fuel, hydrogen, is used.

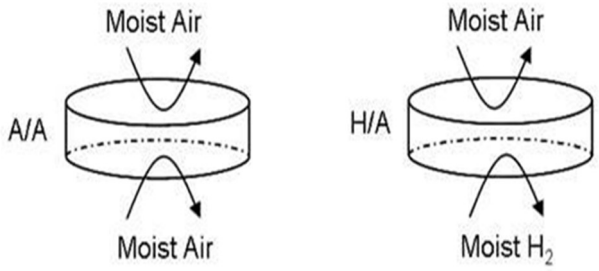

Figure 2.1.1: Schematic of SA and DA exposures (8)

Interconnect Materials

Requirements of the Interconnect

SOFC stacks historically operate at temperatures between 800 and 1000°C. This limited interconnect material selection to YSZ and other ceramic interconnects. Recent advances in SOFC technology has reduced operating temperatures to below 800°C, allowing for previously unviable materials to be investigated for use in SOFC systems. Much research has been done investigating ideal IC properties with regards to SOFC fuel choices and operating conditions. It is generally accepted that the ideal IC material must possess the following qualities (5; 9; 10; 11):

1. Excellent electrical conductivity (<1 Ωcm)
2. Good thermal conductivity (>5 $Wm^{-1}K^{-1}$)
3. Chemically and thermally stable structure

4. Inert with adjacent SOFC components and gaseous environments
5. Exceptionally low permeability for oxygen and hydrogen
6. Compatible coefficient of thermal expansion (CTE) with other SOFC components
7. High temperature strength and creep resistance
8. Easily and cheaply manufacturable

Very few materials meet the functional restrictions of ICs. Currently, the bulkiest component of SOFCs is the IC. Reducing the size, weight, and cost of this component is essential for solid oxide fuel cells to become economically viable as a source of energy production.

Evolution of Interconnect Materials

Until recently, the high operating temperatures of SOFCs required the use of ceramic ICs that were very expensive and difficult to manufacture. Initial research during the late 1960s focused on the use of ceramics such as TiO_2 doped with Ni_2O_5 (12).However, the low thermal expansion did not match the other components, requiring the move to another material. The most popular alternative ceramic material was lanthanum chromite ($LaCrO_3$), and it continues to be the preferred IC material for tubular SOFCs (12; 13). Lanthanum chromite operates well under SOFC operating conditions at temperatures exceeding 800°C; however, substantial degradation of the material is seen below these temperatures (5; 14; 15).Additionally, the low thermal conductivity of rare earth chromites such as $LaCrO_3$ tends to generate thermal gradients within the material, inducing thermal stresses. These restrictions drive research for a suitable replacement to $LaCrO_3$ in high temperature fuel cells. Despite these restrictions on $LaCrO_3$, a great

amount of research continues into different manufacturing techniques and dopants for lanthanum chromite to better match the characteristics needed in a SOFC IC.

While most metal alloys do not work as ICs at the higher end of SOFC operating temperatures, metal alloys are promising for use in intermediate temperature solid oxide fuel cells(650-800°C) (6). Metallic interconnects promise to fulfill the economic desires of IC as cheap and easily manufacturable; however, they often struggle to meet operational requirements under these temperatures. Advantages of metals over ceramics include higher thermal conductivity, greater mechanical stability, low gaseous permeation, and higher electrical conductivity (16). The difficulty arises in that these metallic components must also be chemically, electrically, and mechanically compatible with the SOFC ceramic components.

Metallic Interconnect Materials

Early research into metallic ICs focused on hybrid materials seeking to take the advantages of both ceramic and metal properties by compositing the two into cermets. Varying degrees of success were seen as Siemens-Plansee developed such a specialty composite for IC application containing Cr-Fe-Y_2O_3; however, this has since been discarded due to the volatilization of Cr, poisoning the fuel cell environment and reducing the efficiency of the stack (12). Another promising cermet was an Inconel 600/AL_2O_3 composite but was cancelled for similar reasons (12).

A great deal of recent research into metallic interconnects aims to tailor metal properties through alloying, rather than through ceramic-metal composite materials. Several metal alloys are currently under investigation for use as IC materials, including

Ni-based alloys, Cr-based alloys, and ferritic stainless steels (FSSs).Ni-based alloys have proven strength at high-temperatures, but tend to have a CTE too high for integration with the other fuel cell components. Cr-based alloys are prohibitively expensive and prone to Cr volatilization at high temperature. Until resolution of these issues, FSSs are the most promising candidate among metals for IC applications.

FSS ICs

Out of the commercially available FSSs, chromia-forming FSSs suffer from the fewest drawbacks and may be readily tailored to meet the stringent list of properties for SOFC IC applications through minor alloy additions. The long-term operation of FSS ICs in fuel cells is dependent upon this chromia scale growing slowly to maintain low electrical resistance; additionally, chromia will begin to spall off if it becomes too thick (17; 18; 19; 20). However, even Cr-doped alloys suffer from rapid oxide growth at operating temperatures of solid oxide fuel cells (21). In order to limit the degree of oxidation and form an electrically conductive oxide, FSSs must contain a weight percent of at least 17 percent Cr – at the increased risk of chromium poisoning. Poisoning in fuel cells is the unwanted chemical reaction of components with impurities in the system. Typically, fuel contaminants are the source of impurities; however, component degradation can also introduce impurities. Cr poisoning results when Cr volatilizes, or evaporates, from the surface of the IC and deposits on the adjacent components: the anode and the cathode. In order to stabilize alloys of 17% chromium and minimize the amount of Cr poisoning, Ti and Nb additions are necessary (12; 22).

While chromia-forming FSSs develop a stable, protective oxide at room temperature, the oxide continues to grow at elevated temperatures; thicker oxides tend to decrease the efficiency of stacks by increasing electrical resistance. Additionally, exposure to dual atmosphere at high temperatures (exceeding 750°C) results in accelerated and anomalous iron oxide growth and the formation of hematite nodules on the air side of the fuel cell (23). Hematite is a type of iron oxide, Fe_2O_3, in crystalline form. Iron oxide, in general – and hematite, specifically – has very poor characteristics in terms of electrical conduction and mechanical interaction with the other fuel cell components, resulting in the greatly reduced efficacy of FSSs in this application. The oxide layers developed at high temperatures are known as thermally grown oxides (TGO).

Despite all these concerns and issues with FSS metals, they remain a promising candidate for use in the fuel cell environment, and a great deal of work is underway, exploring the mechanisms behind these detracting characteristics.

Previous Metallic Interconnect Corrosion Research

Single and Dual Atmosphere Effects on FSS Oxidation

When FSSs undergo dual atmosphere exposure, as seen in SOFC IC operation, the TGO layer growth rate is seen to become accelerated and anomalous, exacerbating the issues with hematite formation (23; 24; 25). Studies comparing single and dual atmosphere cases suggest that this growth is likely due to hydrogen transport through the stainless steel. In this transportation, the positively charged hydrogen ions – protons by

another name – fill interstitial sites through the stainless steel, creating a charge differential in the FSS interconnect material. The net positive charge then encourages negative oxygen ion diffusion into the bulk host lattice, in turn, creating cation vacancies in the oxide. These vacancies then enhance the diffusivity of iron cations (Fe^{2+}, Fe^{3+}) from the bulk alloy into the oxide scale where oxygen may readily bond with the iron to create the Fe_2O_3 oxide layer (24; 25). In this manner, the dual atmosphere condition causes the oxide layer to rapidly grow. The method of hydrogen transport through stainless steel is still in need of study, instigating this investigation.

A recent study performed in 2015 (to be published in 2016) by Alnegren et al investigated the effects of dual atmosphere on 0.2 mm thick AISI 441 foil. The researchers saw the development of the same two oxide scales as previously discussed, describing it as “an outward growing hematite phase and an inward growing iron-chromium oxide” (20). In this study, breakaway oxidation of the iron oxide was seen as the coupon experienced chromium depletion. The chromium depletion was presumably an effect of chromium volatilization and only occurred in the dual atmosphere test, suggesting that hydrogen may influence volatilization. The scientists did note that the high flow rate of humid air in this test may also be a constituent. A better understanding of these mechanisms must be developed before materials may be selected for use as SOFC ICs.

A different study compared three promising stainless steel alloys exposed to single and dual atmosphere conditions, noticing a reduction in anomalous oxidation with an increase in chromium content (25). AISI 430 (17 wt. % Cr) and Crofer 22 APU (23

wt. % Cr) experienced accelerated iron transport in the scale when hydrogen was present, resulting in hematite nodules on the surface (25). E-brite, containing 27% Cr, saw little change in oxide scale. Crofer 22 APU and E-brite are specialty FSSs that make use of increased Cr content to reduce the anomalous oxidation; however, this creates a new problem with Cr transport and resultant poisoning of the surrounding fuel cell components. This study will focus on the oxide and microstructure evolution of AISI 441 in regards to the transport of hydrogen through the IC material without a coating (26; 27).

Selection of Ferritic Stainless Steel AISI 441

Ferritic stainless steel AISI 441 is often chosen for dual atmosphere studies due to its availability, composition, and sensitivity to hydrogen exposure (8). AISI 441 was originally designed for the high temperature strength and creep resistance needed for use in car mufflers. Conveniently, this material also possesses the high temperature behaviors desired for implementation with the ceramic SOFC components. Including the manufacturability and cost, AISI 441 is among the top candidates for use as an SOFC IC. Despite its promising candidacy, it has been shown that AISI 441 is particularly sensitive to dual atmosphere exposure, though the causes are not fully known. This sensitivity can be used in research to evaluate the degradation of FSS over reduced time frames and extrapolated to explain issues seen with other FSS ICs.

Figure 2.4.1 and Figure 2.4.2 show the surface oxide as parallel experiments are run on AISI 441 and 430(24). After 200 hours of exposure, the single and dual atmosphere surface oxides appear to be approximately the same on FSS 430 [Figure

2.4.1]. FSS 441, however, shows noticeable change in structure [Figure 2.4.2]. The change in FSS 441 surface oxide is attributed to the formation of a hematite layer on top of the chromia as determined by electron backscatter diffraction spectroscopy (EBSD).

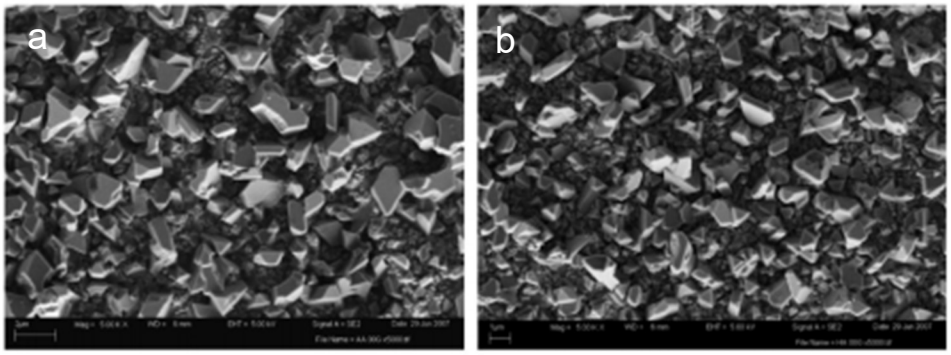

Figure 2.4.1: SEM surface images for AISI 430 exposed to 200 hr 800°C single (a) and dual (b) atmospheres

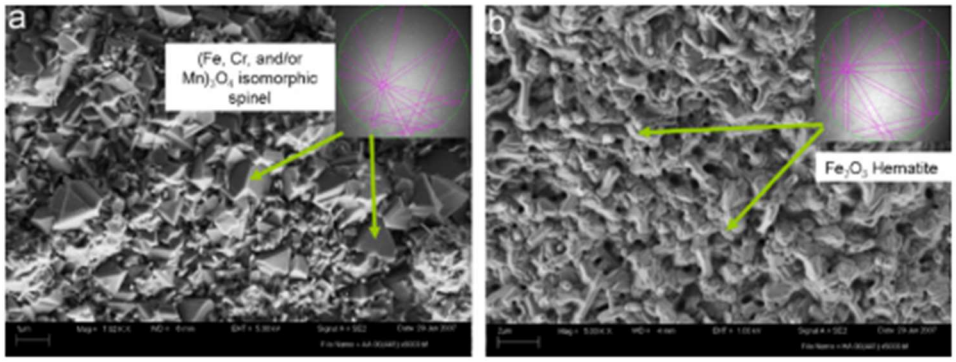

Figure 2.4.2: SEM surface images of FSS 441 with inset selected area electron diffraction (Kikuchi) patterns for single (a) and dual (b) atmosphere exposures

While both the chromia and hematite oxide layers continue to grow during this time, the hematite oxide layer grows much more rapidly [Figure 2.4.3] (24). This oxide formation is concerning as hematite behaves drastically worse than chromia in that it does not possess the desired electrical characteristics – 2.8 Ω·cm when under 1 Ω·cm is

desired –limiting its efficacy for use as an interconnect material solid oxide fuel cell systems(28). Additionally, these iron oxides are less protective and oxidize several orders of magnitude faster than chromium oxide (20).

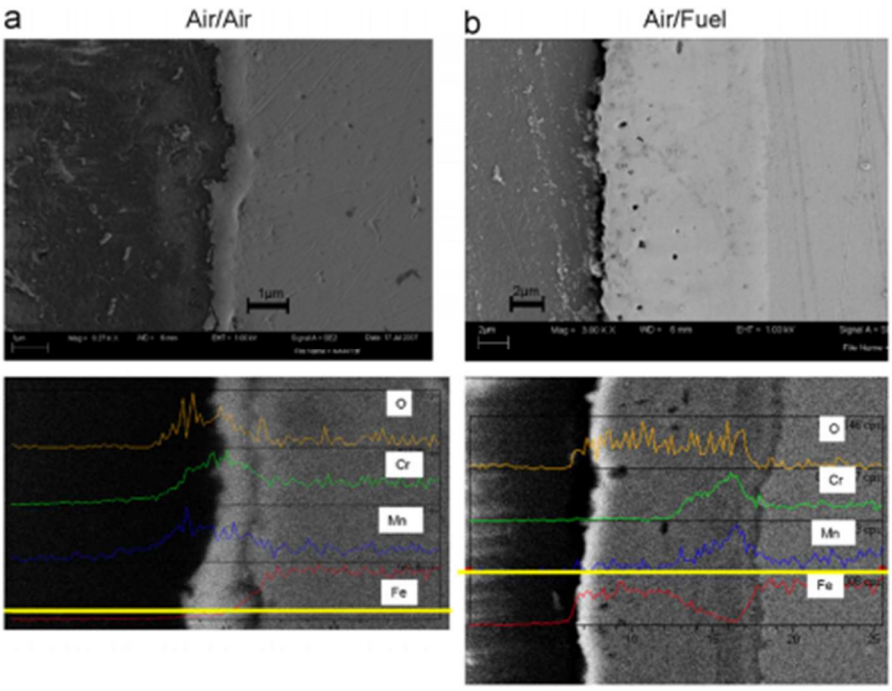

Figure 2.4.3: SEM cross-section images with EDS line scans of FSS 441 after 200 hr, 800°C single (a) and dual (b) atmosphere exposures – different magnifications. (24)

Impact of Moisture on TGO

In conjunction with the series of single and dual atmosphere tests, the effect of moisture were also investigated; a very important aspect when considering water is created in the fuel cell reaction. The effects of water on oxidation of iron-chromium alloys have been researched for decades and are a complicated phenomenon. One study of water vapor induced oxidation of Fe-Cr alloys found alloys containing less than 15 weight percent Cr saw linearly increasing oxide growth between 800 and 1100 °C (29).

In this study a wustite (FeO) outer layer and wustite-spinel sub-layer were observed with a notable separation between and within the oxide scales [Figure 2.4.4].

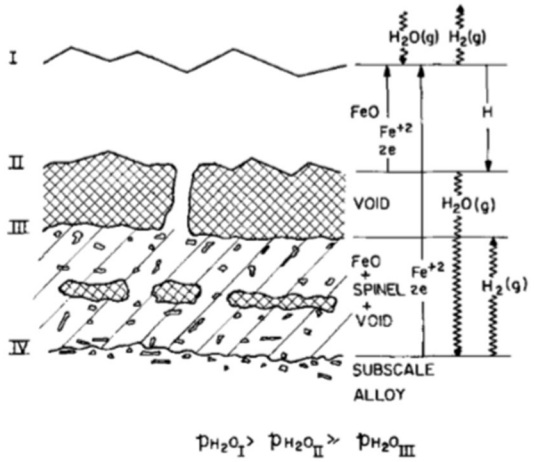

Figure 2.4.4: Proposed mechanism for the oxidation of Fe-Cr alloys in water vapor at high temperatures (29)

The proposed mechanisms for the continued oxidation growth can be seen in the following reactions for each oxide layer. In the following expressions, H^* refers to hydrogen dissolved in the oxide. The hydrogen notation is intentionally left ambiguous as this was suspected to be ionized, but no proof was available.

Equation 3: Interactions at the I Surface

$$H_2O_{(g)} \Leftrightarrow H_2O_{(ads)}$$
$$H_2O_{(ads)} + Fe_C^{\bullet\bullet} + 2e' \rightarrow FeO + V_{Fe}'' + 2h^{\bullet} + H_{2(ads)}$$
$$H_{2(ads)} \Leftrightarrow H_{2(g)}$$
$$H_{2(ads)} \Leftrightarrow 2H_{(ox)}^*$$

Equation 4: Interactions at the II Surface

$$FeO + V_{Fe}'' + 2h^{\bullet} \Leftrightarrow Fe_C^{\bullet\bullet} + O_A''$$

$$2H^{*}_{(ox)} \Leftrightarrow H_{2(ads)}$$
$$H_{2(ads} \Leftrightarrow H_{2(g)}$$
$$H_{2(ads)} + O''_{(ads)} \rightarrow H_2O_{(g)} + 2e'$$

As can be seen, the researchers behind water vapor oxidation study were concerned with the permeation of hydrogen at this juncture and how this permeation could propagate oxidation into sub-layers. Other proposed reactions exist in the source paper with regards to oxidation of the spinel layer, but were left out of this thesis.

Even with high chromium contents, Fe-Cr alloys form porous iron-rich oxide scales with hematite nodules in high water content environments, indicating this is yet another factor that must be controlled while designing SOFC systems (30).

Ferritic Stainless Steel

Microstructural Evolution

Ferritic stainless steels are characterized by the body centered cubic (BCC) crystalline structure. In general, this structure is known to be ductile and resistant to crack propagation. BCC-type materials are generally hardened with interstitial solutes as seen with the minor alloying additions of FSS 441 (31).

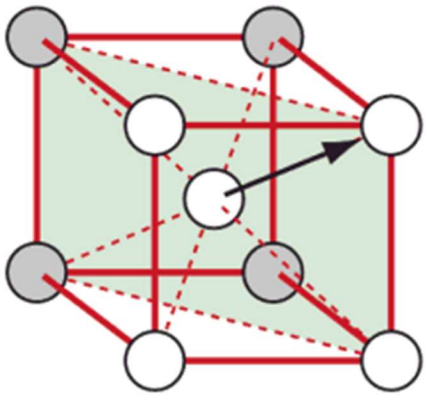

Figure 2.4.5: Unit Cell of Body Centered Cubic Crystalline Structure (31).

Many high temperature metals use minor alloying additions to improve the mechanical properties by solid solution hardening (32). A major difference between AISI 441 and other stainless steel alloys is the formation of Laves phase precipitates between 600 and 900°C.This encompasses the operating temperature of intermediate temperature SOFC stacks, meaning these Laves phase precipitates must be considered while evaluating the diffusion of hydrogen through FSS 441.The volume fraction of Laves phase precipitates is maximum at 850°C (33).AISI 441 Laves phase precipitation is driven by the minor alloying addition of Nb, instigating Fe_2Nb formation; only AISI 441 containing Nb minor alloying additions will see the formation of Laves phase precipitates.

Laves phase is a specific type of intermetallic phase. In AISI 441, the Laves phase composition is Fe_2Nb; this type of Laves phase is commonly known as AB_2. The C15 Laves phase structure shown is a body centered cubic structure and among the most common crystalline structures, however, other structures are frequently exhibited [Figure 2.4.6]. Hexagonal is another common Laves phase crystalline structure.

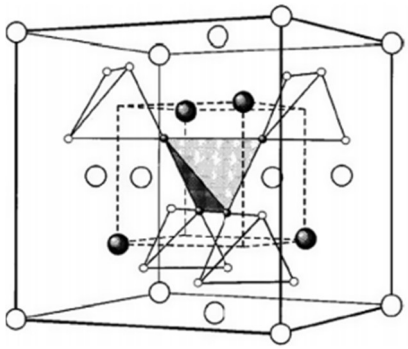

Figure 2.4.6: AB_2 Laves Phase Structure C15. The large symbols are the A component and the small symbols are the B component. The broken lines and shaded symbols indicate one primitive cell. (34)

Historical Laves Phase Research of FSS

Studies have been performed in the past establishing the effects of solid solution hardening on the mechanical and creep characteristics of stainless steels in high temperature, single atmosphere applications, such as catalytic converters and exhaust systems. Conversely, the amount of research on the effects of Laves phase in dual atmosphere environments is comparatively small. In single atmosphere testing, the volume fraction of precipitated Laves phase reaches maximum volume percent at around 1000 minutes, just over 16 hours, even at the relatively low temperature of 600°C; at higher temperatures, saturation is met much more quickly [Figure 2.4.7] (32).

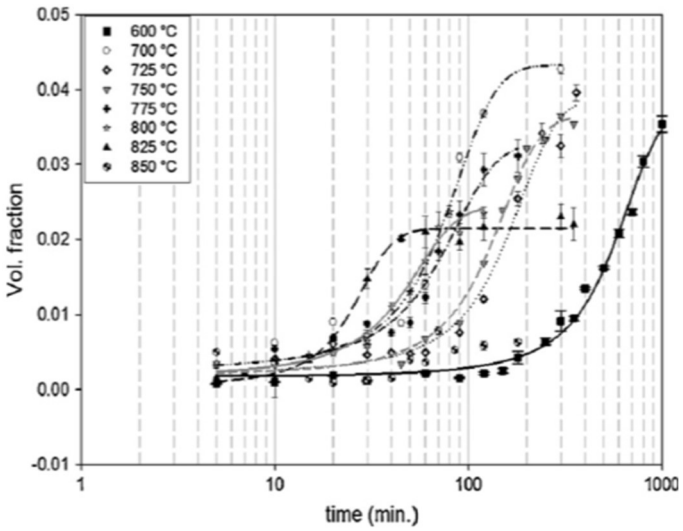

Figure 2.4.7: The Laves Phase Volume Fraction – Temperature/Time Curves during Isothermal Annealing of AISI 441 in SA (32)

Hydrogen storage research has explored the effects of Laves phase on hydrogen adsorption and desorption. Ti-based alloys have shown significant improvement in hydrogen adsorption and desorption by inducing Laves phase precipitation in bcc-structures with Nb additions (35). Other studies have looked at metal hydrides,

particularly AB_5 and AB_2Laves phase, for hydrogen storage purposes seeing high hydrogen capacities and high hydrogen equilibriums (36). One study has even correlated the stabilities of metal hydrides and the radii of interstitial holes in AB_5 and cubic AB Laves phase structures (37). As such, it is of particular note that precipitates of this phase existent within and throughout a material chosen for fuel cell application.

CHAPTER THREE

EXPERIMENTAL PROCEDURE

Sample Preparation and Definition

Two different thicknesses – 0.5 and 1.2 mm – of AISI 441 FSS were tested under several different atmosphere conditions to assess the microstructural evolution with the goal to investigate and possibly relate thermally grown oxide layer and Laves phase development. The batch composition for each thickness is shown in Table 3.1.1 as given by National Kwikmetal Service (0.5 mm sheet) and Alleghany Ludlum (1.2 mm sheet). Rectangular and circular coupons were laser cut from sheets and ultrasonically cleaned in order to remove manufacturing oils.

Table 3.1.1: Batch Composition for AISI 441 FSS Alloys as Stated by Manufacturer

Thickness	**Nominal composition (wt. %)**										
(mm)	**Fe**	**Cr**	**Nb**	**Si**	**Mn**	**Ti**	**Ni**	**Cu**	**Al**	**P**	**Co**
0.5	Bal	17.99	0.612	0.41	0.28	0.273	0.15	0.12	0.035	0.026	0.02
1.2	Bal	17.8	0.500	0.32	0.3	0.18	0.3	0.11	0.04	0.03	--

Single Atmosphere Experimental Procedure

Single atmosphere (SA) tests were performed in order to assess the effect of high temperature and oxidizing environment on the microstructural evolutions of the AISI 441. Rectangular samples of 0.5 and 1.2 mm thickness were exposed to 800°C, stagnant air in a muffle furnace for 24, 48, 72, and 100 hours. The heating ramp was approximately 3 degrees/minute and the testing temperature was reached over the period of 5 hours. The cooling process was also performed with about 3 degrees/minute ramp and ambient temperature was reached over the same time frame.

Dual Atmosphere Experimental Procedure

Multiple dual atmosphere experiments were performed in order to investigate the influence of specific parameters on the microstructural development of FSS AISI 441. Two 25mm diameter coupons of each thickness were exposed per each test. The testing apparatus was developed from a design by the National Energy Technology Laboratory in Albany, OR [Figure 3.3.1 & Figure 3.3.2] (38). The hydrogen (or hydrogen mixture) ran through the channels labeled Gas 1 and Gas 2. Air was used for Gas 3 inside the alumina tube but outside of the mounting apparatus.

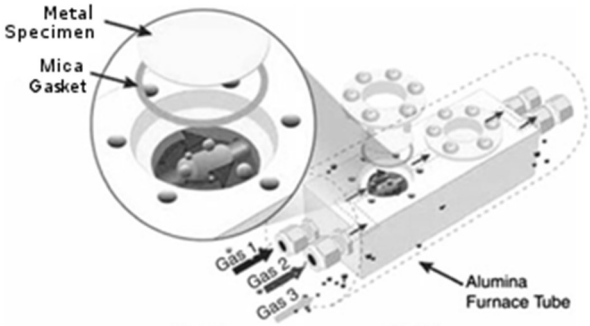

Figure 3.3.1: Dual atmosphere coupon mount

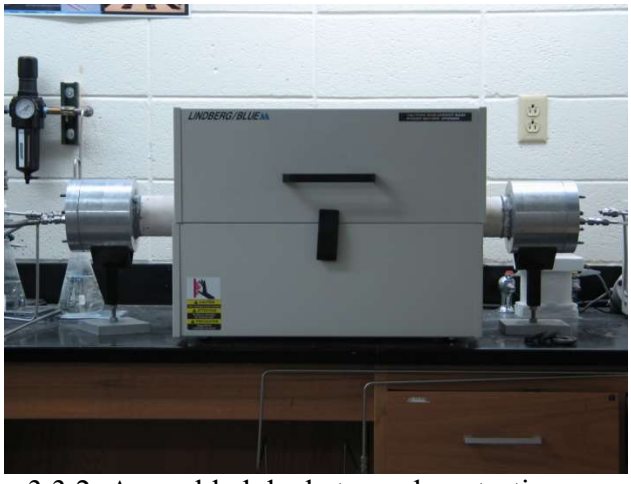

Figure 3.3.2: Assembled dual atmosphere testing apparatus

Tests were performed at 800°C and for various time intervals: 24, 48, 72, and 100 hours. When moist gases were required, 3 vol. % moisture was realized by passing the gasses through a humidifier which contained H_2O at room temperature (~20 °C). The humidifier was placed close to the entrance to the furnace; therefore, the gases were first enriched with water vapor before contacting the samples. The inlet gases were not preheated before entering the testing environment. Gas flow rates were maintained near 60 sccm for air and 30 sccm for hydrogen. Alumina silicate (mica) O-rings, which are being considered for use as gaskets in planar SOFC stacks, were utilized to create a

hermetic seal throughout the rig. The apparatus was leak tested with He gas before the dual atmosphere exposures. Selected conditions are listed below:

- Dual atmosphere (DA): for this test moist gases (air and pure hydrogen) were used. The test was performed in order to confirm the accelerated anomalous oxidation phenomenon and to investigate the Laves phase evolution in conditions as close as possible to the SOFC working environment.
- Dual atmosphere with different hydrogen partial pressure (DA PP): as in the first case, moist gases were used but instead of pure hydrogen a 5 H_2: 95 Ar mixture was used. This test aimed to assess the effect of a lower hydrogen pressure on the steel oxidation and Laves phase evolution.
- Dry gases dual atmosphere (DA dry): both inlet gases were not humidified before reaching the samples. Comparing the results with those of the above listed conditions, this test aimed to assess the effect of water vapor on the steel oxidation and Laves phase evolution.

Vacuum Experimental Procedure

For the vacuum testing, rectangular coupons were placed within a vacuum furnace. An alumina crucible was used to hold the coupons throughout the duration of the test. After the furnace reached its maximum vacuum, the furnace was heated to 800°Cover five hours (3°C / min) and was maintained for 100 hours. Following a five hour cooling ramp down to room temperature, the pressure was returned to ambient. The

purpose of this test was to explore the effects of temperature on the steel oxidation and Laves phase evolution without the influence of the various environments.

Metallographic Sample Preparation

Analysis of the Laves phase precipitation is dependent upon viewing the metallographic structure via microscopy techniques. Samples undergoing metallographic analysis were prepared with EpoxyBond 110 and glass then cross-sectioned with the Techcut 7 Precision Sectioning Machine before mounting according to the epoxy sandwich mount method as seen in Figure 3.5.1 (39).The samples were polished on the TECHPREP Multiprep Polishing System. The metallographic polish technique developed in conjunction with Allied High Tech, Inc. is outlined in Table 3.5.1(40). Steps 11 and 12 were only performed when analysis was being performed without etching as in EBSD. Samples were analyzed after polishing for establishing oxide thicknesses and various elemental analyses. For FESEM images of the microstructure, etching was performed using agent Glyceregia (15cc HCl, 10cc Glycerol, 5 cc HNO_3).

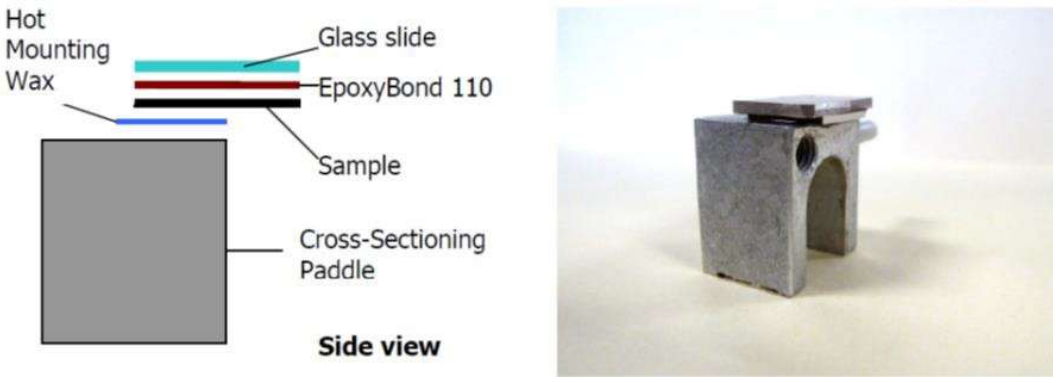

Figure 3.5.1: Epoxy Sandwich Mounting Method for Sample Preparation (39)

Table 3.5.1: Metallographic Polishing Procedure (40)

Step	Grid Size	Type	Carrier	Coolant	Platen Speed (RPM)	Sample Load	Time
1	320 Grit (45 µm)	SiC	Abrasive Discs	Water	200/CCW	500g	As needed
2	480 Grit (35 µm)	SiC	Abrasive Discs	Water	200/CCW	500g	5 min
3	600 Grit (30 µm)	SiC	Abrasive Discs	Water	200/CCW	500g	5 min
4	800 Grit (25 µm)	SiC	Abrasive Discs	Water	200/CCW	500g	5 min
5	12 µm	$\mathbf{Al_2O_3}$	Lapping Film	Red Lube	150/CCW	500g	5 min
6	9 µm	$\mathbf{Al_2O_3}$	Lapping Film	Red Lube	150/CCW	500g	5 min
7	5 µm	$\mathbf{Al_2O_3}$	Lapping Film	Red Lube	150/CCW	500g	5 min
8	3 µm	$\mathbf{Al_2O_3}$	Lapping Film	Red Lube	150/CCW	500g	5 min
9	1 µm	$\mathbf{Al_2O_3}$	Lapping Film	Red Lube	150/CCW	500g	5 min
10	0.3 µm	$\mathbf{SiO_2}$	Microcloth	Suspension	150/CCW	500g	2-5 min
11	0.1 µm	$\mathbf{SiO_2}$	Microcloth	Suspension	150/CCW	500g	2-5 min
12	0.05 µm	$\mathbf{SiO_2}$	Microcloth	Suspension	150/CCW	500g	2-5 min

Analytic Techniques

FE-SEM

A Zeiss Spura 55VP Field Emission Scanning Electron Microscope (FE-SEM) was used for the majority of analysis on samples and surface oxides throughout this study. High quality imaging was performed on polished and etched cross sections at 5-7 mm and 5kV, per ICAL suggestion. FE-SEM built-in systems were used for further analysis. Energy-dispersive x-ray (EDX) spectroscopy was used for spot and line scans at 3k magnification, using a working distance of 11mm and voltage of 20 kV. Additional

compositional analysis was performed on polished, non-etched samples using electron backscatter diffraction (EBSD).

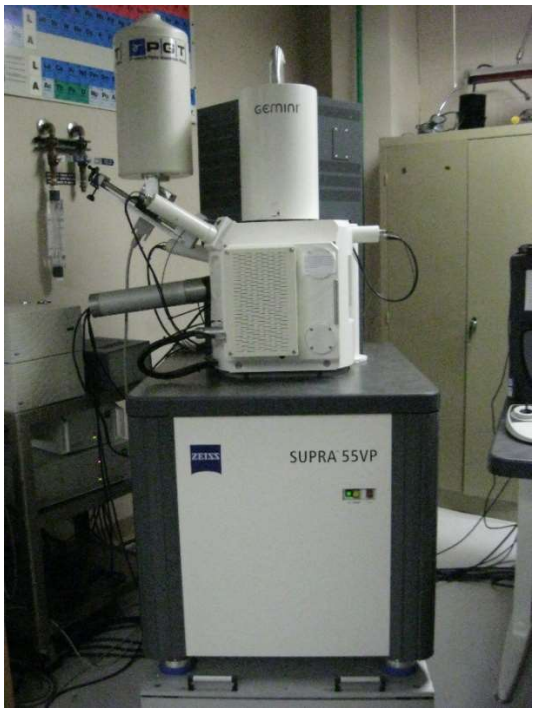

Figure3.6.1: Zeiss Spura 55VP Field Emission Scanning Electron Microscope

Scanning Electron Microscope

A JEOL JSM-6100 Scanning Electron Microscope (SEM) was used to perform additional testing on the cross section of AISI 441 after Laves phase precipitation. An SEM component, the Energy-Dispersive x-ray Spectrometer (EDS), allows for more precise measurement of elemental compositions at points, line scans, and two-dimensional mapping to an accuracy of 1-2%. Another technique used was the Backscattered Electron Imaging (BEI) to image with regards to different atomic weights

of elemental components. BEI was done at 3k magnification at a power of 15kV and a working distance of 37mm (41).



Figure3.6.2: JEOL JSM-6100 Scanning Electron Microscope

ImageJ Analysis Technique

Analysis of percent surface area Laves phase was conducted via ImageJ analysis. The etching method chosen left behind the precipitates that form within AISI 441 at high temperatures. The height and other geometric differences led to the Fe_2Nb Laves phase precipitates to be highlighted as bright nodules decorating the sample cross-section. ImageJ allows the contrast differences to be emphasized and isolated to show only the nodules. This powerful technique can be used to optically evaluate the percent of Laves phase that covers a cross-sectional area. In addition, the location of the nodules can be more easily determined (grain or grain boundary). An image that underwent analysis via ImageJ is shown in Figure 3.6.3.

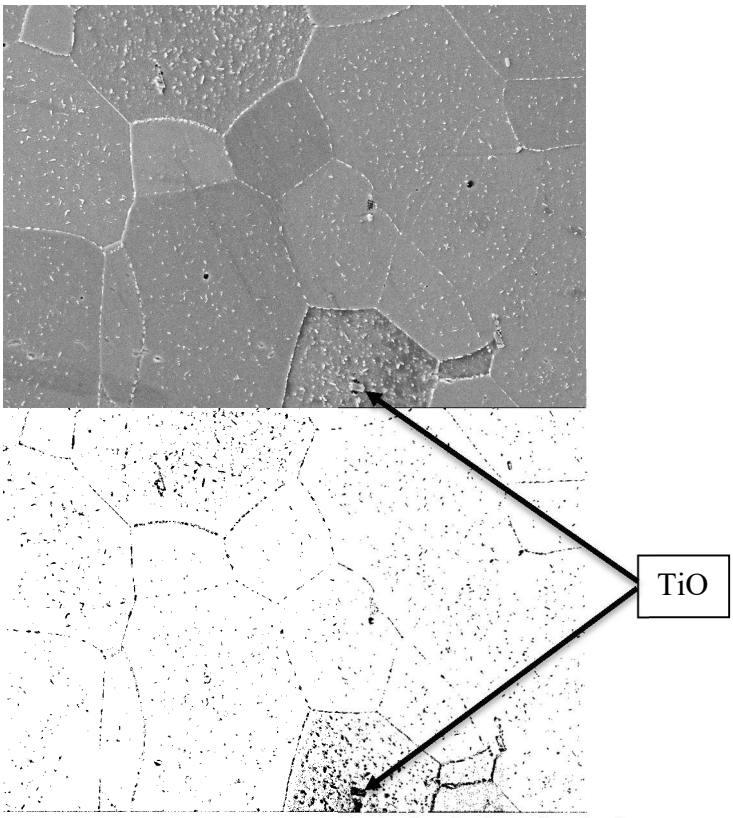

Figure 3.6.3: Image before and after ImageJ Manipulation for Isolating Nodules

A major downside to this technique is that any feature appearing bright in the SEM base image may be isolated and included in the nodule count; this can include features such as other precipitate nodules or steeply etched grain boundaries. An example of a titanium oxide nodule being included in the ImageJ analysis can be seen in Figure 3.6.3. Large geometries – particularly at grain boundaries – that can affect the area percent measurement of Laves phase are shown in Figure 3.6.4; a 1.2mm sample exposed to SA for 72 hours. This image was selected for its large number of features that are not precipitates. Note “a” points out the slope generated between two grains etching at different rates. Note “b” indicates one specific grain that saw variations in geometry within the grain. In some cases the differences in geometry can be attributed to polishing

and etching flaws. It is possible to avoid many of these geometrical differences, but impossible always avoid them.

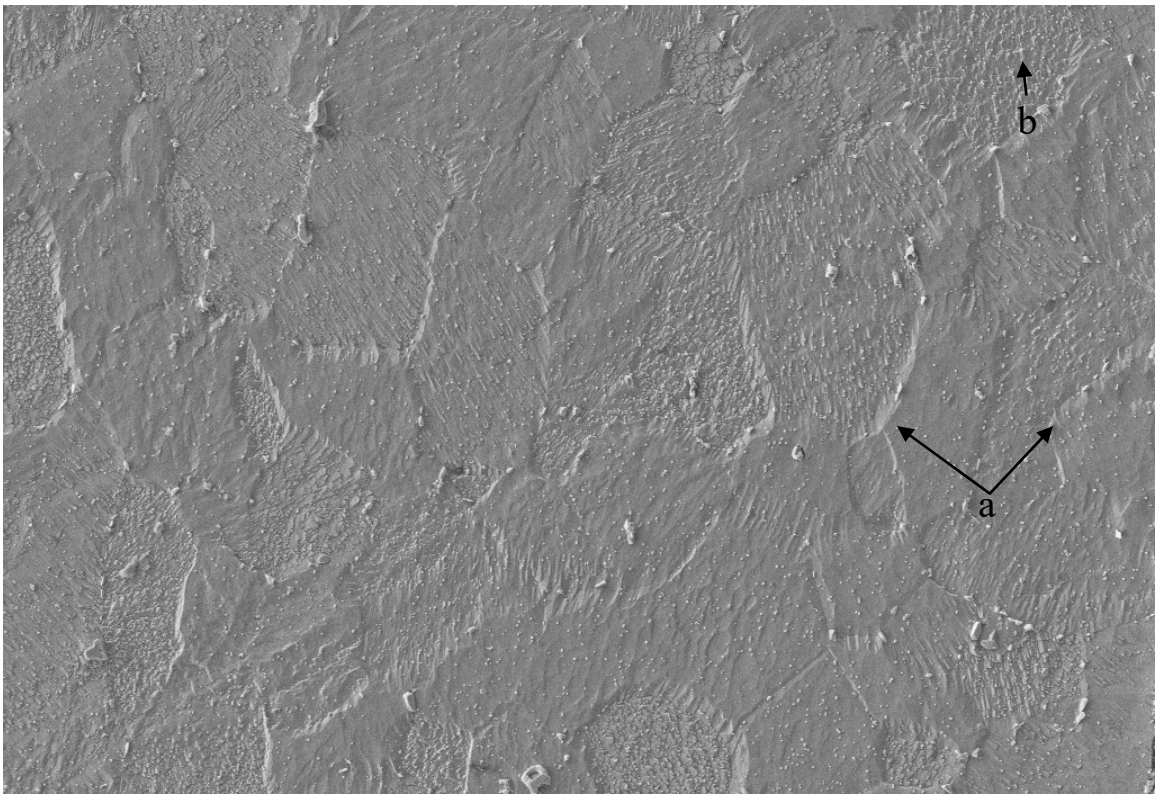

Figure 3.6.4: 1.2mm SA cross-section with large geometries: a) slope between grains, b) general roughness after etching.

As such, the limited inclusion of non-pertinent surface features must be taken into account. To mitigate incorrect counts due to these geometries, the images must either be carefully selected to include only the precipitates of interest or, more practically, the image must be modified to remove features that are not of interest. Thus the process can yield slightly different area percent values for the same image being analyzed by two different users. To limit this error basis on this study, one person performed all the

analysis and a 95% confidence interval is utilized to evaluated differences among the different test environments.

CHAPTER FOUR

RESULTSAND DISCUSSION

The Initial Detection Precipitates

This query formed after the initial dual-atmosphere testing was performed on 0.5 mm AISI 441 for 100 hours at 800°C and compared to the as-received sample. The cross-section of the as-received sample possessed a mostly homogeneous surface; however, bright nodules decorated the grains and grain boundaries of the DA cross-section [Figure 4.1.1]. The apparent concentration of nodules along grain boundaries raised the question, "Could these precipitates facilitate hydrogen movement through AISI 441?"

Electron Backscatter Diffraction

Electron Backscatter Diffraction (EBSD) was used during this study as another potential method for distinguishing the existence of the Laves phase precipitates from the stainless steel matrix by means of crystallographic differences. One attempt at EBSD mapping can be seen in Figure 4.1.2 where software was used to identify Kikuchi patterns. Red was used to note the location of AISI 441 and the blue to note AB_2 Laves phase precipitate structure.

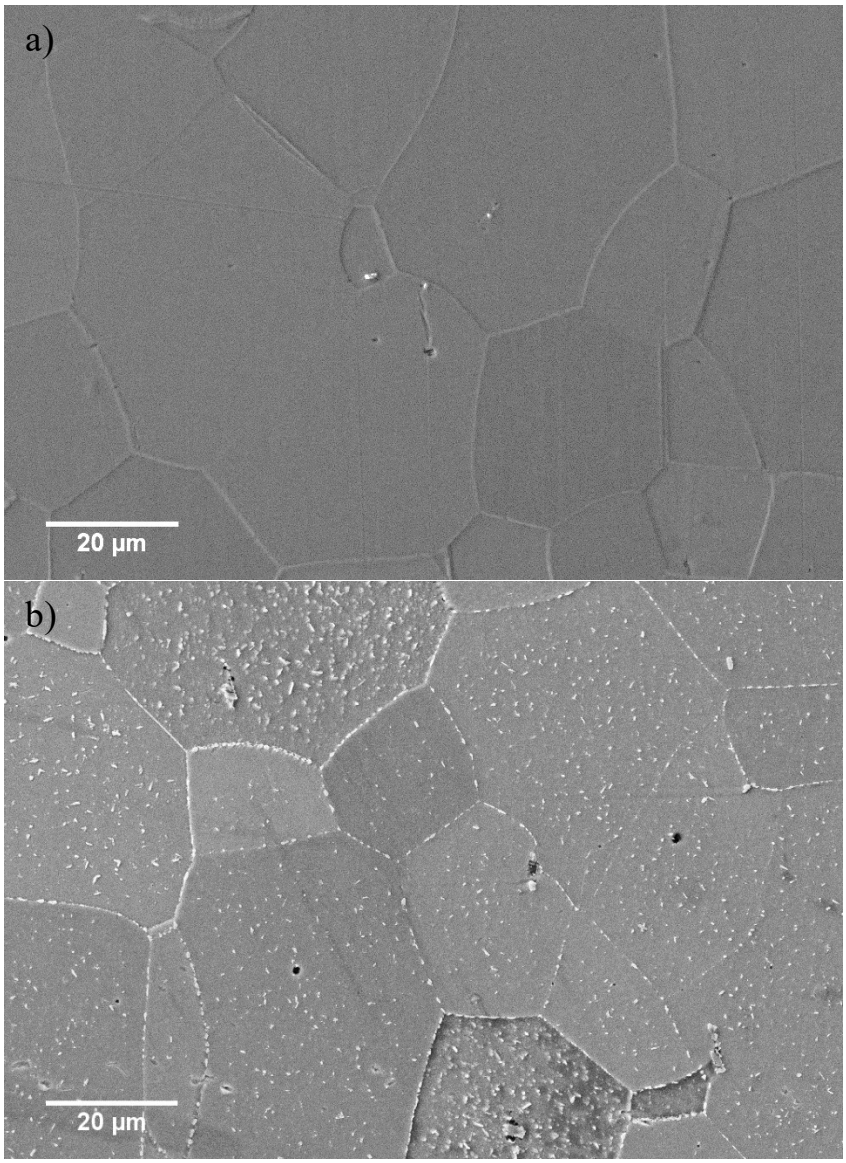

Figure 4.1.1: FE-SEM microstructure images taken of 0.5 mm thick AISI 441 samples after etching a) as-received and b) dual-atmosphere specimens

If the software could not identify the response as a particular crystal orientation, the location was colored green. This can be seen along every grain boundary where the difference in crystallographic orientation between the grains of the matrix material was sufficiently different to result in a null reading. Considering that this system did not give

reliable readings along these relatively large grain boundaries, pursuit of this EBSD system for identification of the much smaller precipitates was deemed nonsensical. As such, ImageJ analysis of electron microscope images was determined to be the most reliable method available for precipitate measurement.

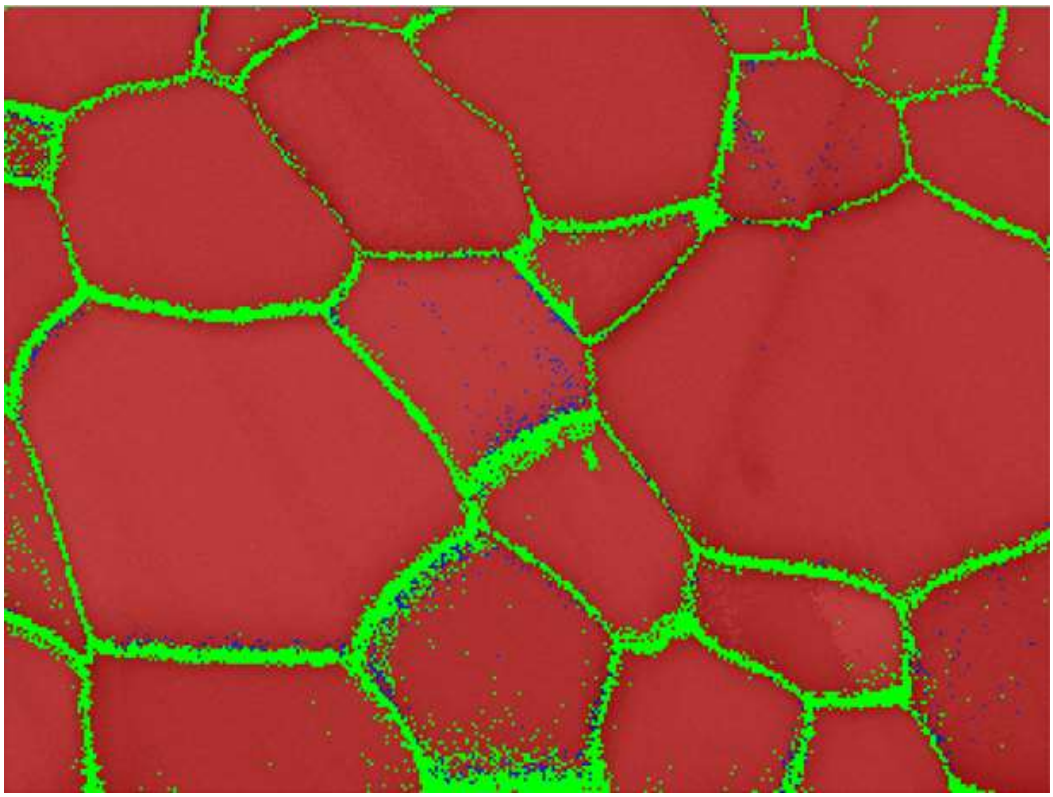

Figure 4.1.2: Electron Back Scatter Diffraction Image to Detect Laves Phase

Microstructural Analysis

As-Received Samples

Comparing the grain sizes of the as-received samples shows a significant difference between the 0.5 and 1.2 mm thick samples [Figure 4.2.1].The planimetric procedure was used for calculating grain size (42). The average grain size in the 0.5 mm

thick sample is 26 μm while the 1.2 mm thick sample has an average grain size of 13 μm. Additionally, the grain sizes of the 0.5 mm sample are more uniform than the 1.2 mm sample where a much greater variation in size exists [Figure 4.2.1]. The variation in grain size is likely attributable to cold working and heat treatment during the manufacturing process. This study does not reach annealing temperatures for AISI 441 and will not attempt to recrystallize the samples to reach a more uniform grain size between the thicknesses. However, this difference in microstructure is noted and considered throughout the analysis of results.

In addition to the grains of the bulk alloy, both as-received samples exhibit precipitate nodules. These precipitates were known to exist as their formation was driven to augment the high temperature characteristics of AISI 441. In these control samples, the 0.5 mm sample is seen to have a 0.03 percent surface area covered with precipitates while the 1.2 mm sample is seen to be 1.3 percent. More precipitates can be seen on the as-received 1.2 mm thick sample; again, the amount of precipitates is likely due to heat treatment during the manufacturing processes. A previous study has noted that the temperature range of precipitate formation in AISI 441 is between the ranges of 600 and 900 °C (32).

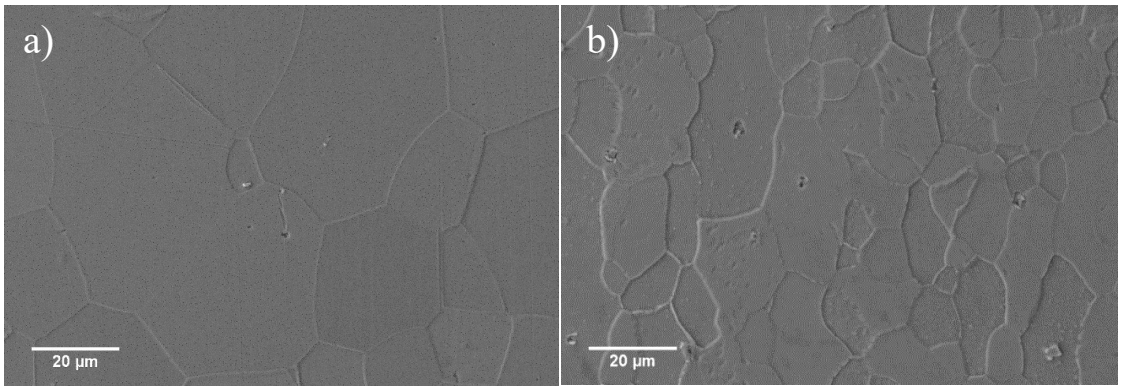

Figure 4.2.1: As-received samples of thickness a) 0.5 mm and b) 1.2 mm

Single Atmosphere Exposure

Metallographic analysis of both thicknesses after SA exposure shows a great increase in the amount of Laves phase precipitation when compared to the as-received samples of the same thickness [Figure 4.2.2]. The 0.5 mm sample appears to have a greater amount as well as larger Laves phase precipitates than the 1.2 mm sample after undergoing the same furnace treatment for 100 hours. Additionally, the precipitate location appears significantly different between the two samples. The 0.5 mm sample shows precipitate concentrations along all of the grain boundaries with a scattering throughout the grains. The 1.2mm sample is observed to have nodules more uniformly spread throughout the grains without the same concentration at grain boundaries and the precipitate nodules are not seen in every grain. ImageJ analysis reveals the 0.5 mm has, on average, 1.6 percent of the surface area covered in precipitates while the 1.2 mm sample is at 1.7 area percent. Despite the apparent differences in Laves phase precipitation, both samples after SA testing are seen to have approximately the same quantity of precipitates.

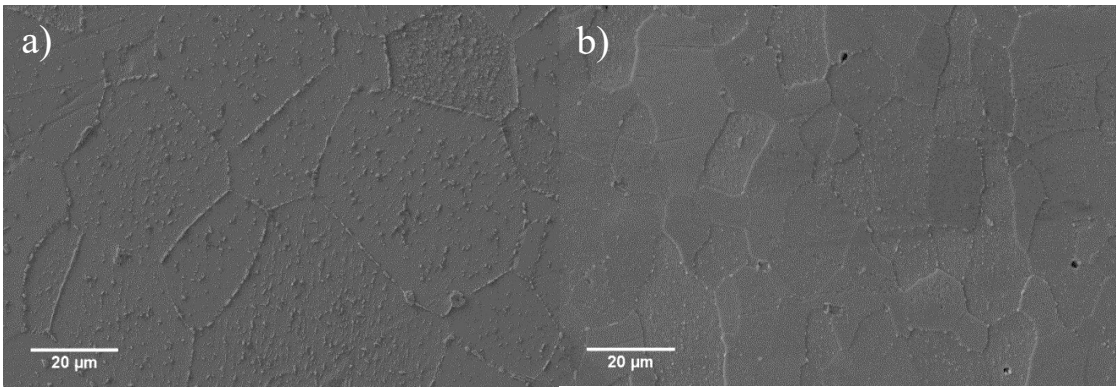

Figure 4.2.2: Single atmosphere exposure for 100 hours on thicknesses a) 0.5 mm and b) 1.2 mm

Dual Atmosphere Exposure

The samples that have undergone DA exposure appear to have a similar amount of Laves phase precipitates as the SA samples after 100 hours [Figure 4.2.3]. Again, the 0.5 mm sample appears to have a particularly high concentration of the nodules along grain boundaries when compared to the 1.2 mm sample. The surface area percentages of the Laves phase precipitates are 1.9 percent for the 0.5 mm thick coupon and 1.9 percent for the 1.2 mm thick coupon. As expected these area percents are very close to the 1.6 and 1.7 area percents seen in the SA exposure testing. As stated earlier, not all nodules and voids seen in the sample cross-section are Laves phase precipitates, although most precipitates are.

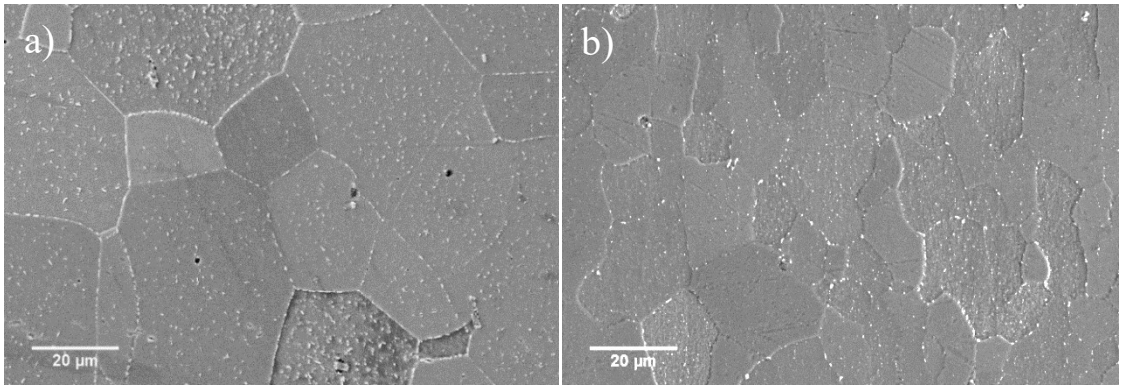

Figure 4.2.3: Dual atmosphere exposure for 100 hours on thicknesses a) 0.5 mm and b) 1.2 mm

Energy-dispersive x-ray spectroscopy (EDX) of selected nodules allowed for preliminary analysis of nodule composition, showing the bright nodules to be largely comprised of niobium, silicon, and oxygen with significantly reduced levels of iron and chromium relative to the alloy composition. Additionally, dark voids and larger nodules were observed and found to contain high percentages of iron, oxygen, and titanium [Table 4.2.1 & Figure 4.2.4].

The composition of the nodules is not an exact measurement due to the resolution and penetration of the measurement, taking the area around the nodule into account for calculating elemental composition. Other studies have given the chemical formula for the smaller nodules as Fe_2Nb which is corroborated by the following EDX analyses [Table 4.2.1] (32). The larger nodules are TiO that is known to precipitate in AISI 441 stainless steel.

Table 4.2.1: Average Qualitative Elemental Composition of Features for AISI 441 FSS Alloys

	Atomic Percent					
Features	**Fe**	**Cr**	**Nb**	**Ti**	**Si**	**O**
AISI 441 Nominal Composition	Bal.	17.99	0.612	0.273	0.410	--
Secondary Phase Precipitates on Grain Boundary (Figure 4.2.4a)	62.35	12.75	3.35	1.14	2.58	17.81
Secondary Phase Precipitates within Grain (Figure 4.2.4b)	63.75	15.02	1.89	0.24	1.71	17.39
Large Nodule within Grain (Figure 4.2.4c)	16.19	5.09	2.03	31.53	1.57	43.59

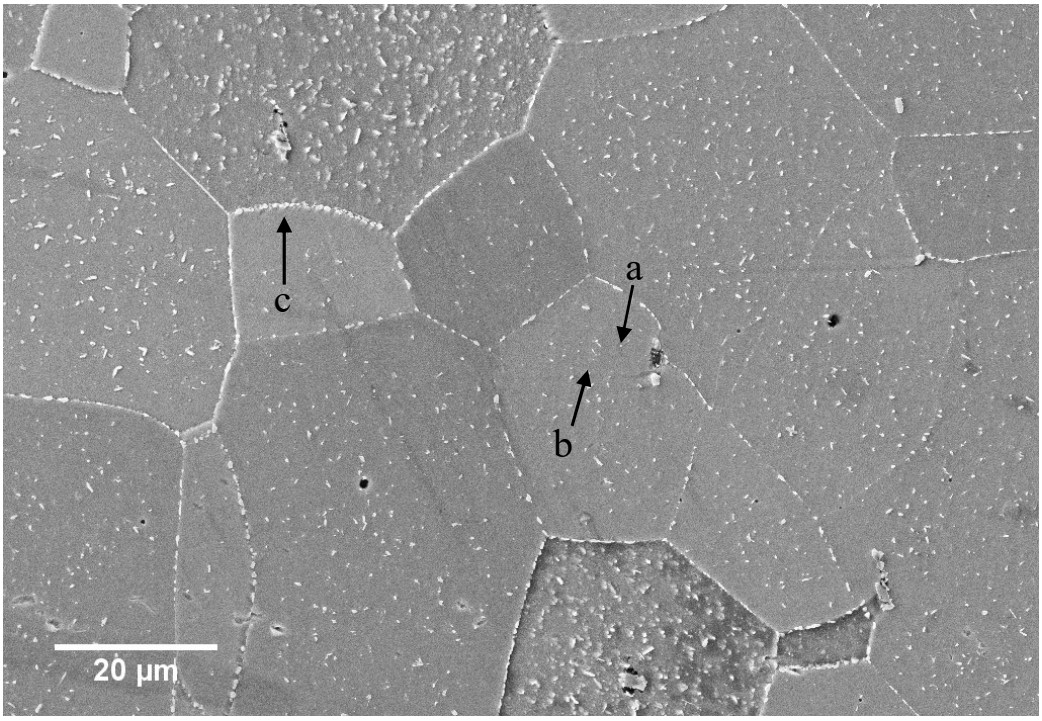

Figure 4.2.4: Energy dispersive x-ray spectroscopy scan locations of FSS 441 cross-section at a) grain boundary precipitate, b) intra-grain precipitate, and c) large nodule.

Vacuum Furnace Heat Treatment

In order to better establish a baseline for the amount of Laves phase precipitates that develop without assistance from the environment, samples underwent heat treatment in a vacuum furnace at 800°C. From optical microscopy, the 0.5 mm thick coupon has nodules all along the grain boundaries [Figure 4.2.5]. The precipitates in the 1.2 mm thick coupons are not quite as concentrated along the grain boundaries, however, enough of the precipitates fall along the grain boundaries that the individual grains can be distinguished via location of precipitates [Figure 4.2.5].This is contrary to the initial thought that the 1.2 mm precipitates do not fall along the grain boundary as frequently as in the 0.5 mm sample.

The area percent covered in these precipitates are 1.9 percent for the 0.5 mm sample and 1.0 percent for the 1.2 mm sample. This matches the area percent of the 100 hour SA and DA tests on the 0.5 mm thick sample. For the 1.2 mm samples, the area percent seen from the vacuum test is lower than any other test, including SA, DA, and as-received. This difference may be attributed to the specific area selected for testing.

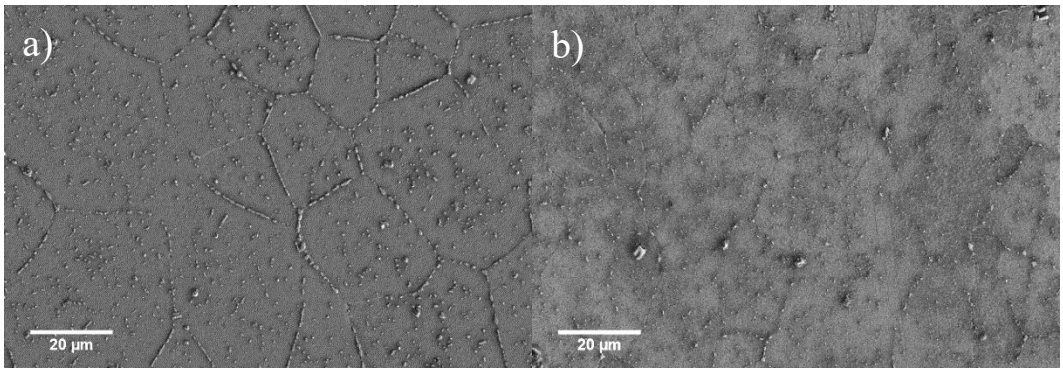

Figure 4.2.5: Samples exposed to 800°C in a vacuum furnace for 100 hours on thicknesses a) 0.5 mm and b) 1.2 mm

Surface Oxide Evolution

As-Received Protective Chromium Oxide

A protective chromium oxide layer was observed on both as-received sample thicknesses. Images of the oxides on the 0.5 and 1.2 mm samples may be seen in Figure 4.3.1 and Figure 4.3.2. The average thickness of the 0.5 mm samples was found to be 0.19 μm and a maximum of 0.26 μm was observed. The 1.2 mm sample average oxide this is 0.11 μm with a maximum thickness of 0.13 μm. EDX line scans were performed on these cross-sections, but the resolution of each measurement step was not high enough to dependably represent the composition of the oxide layer. A sample line scan accompanies each figure, but analysis of the surface oxides prior to environmental exposure will serve to establish the base-line of the oxide composition.

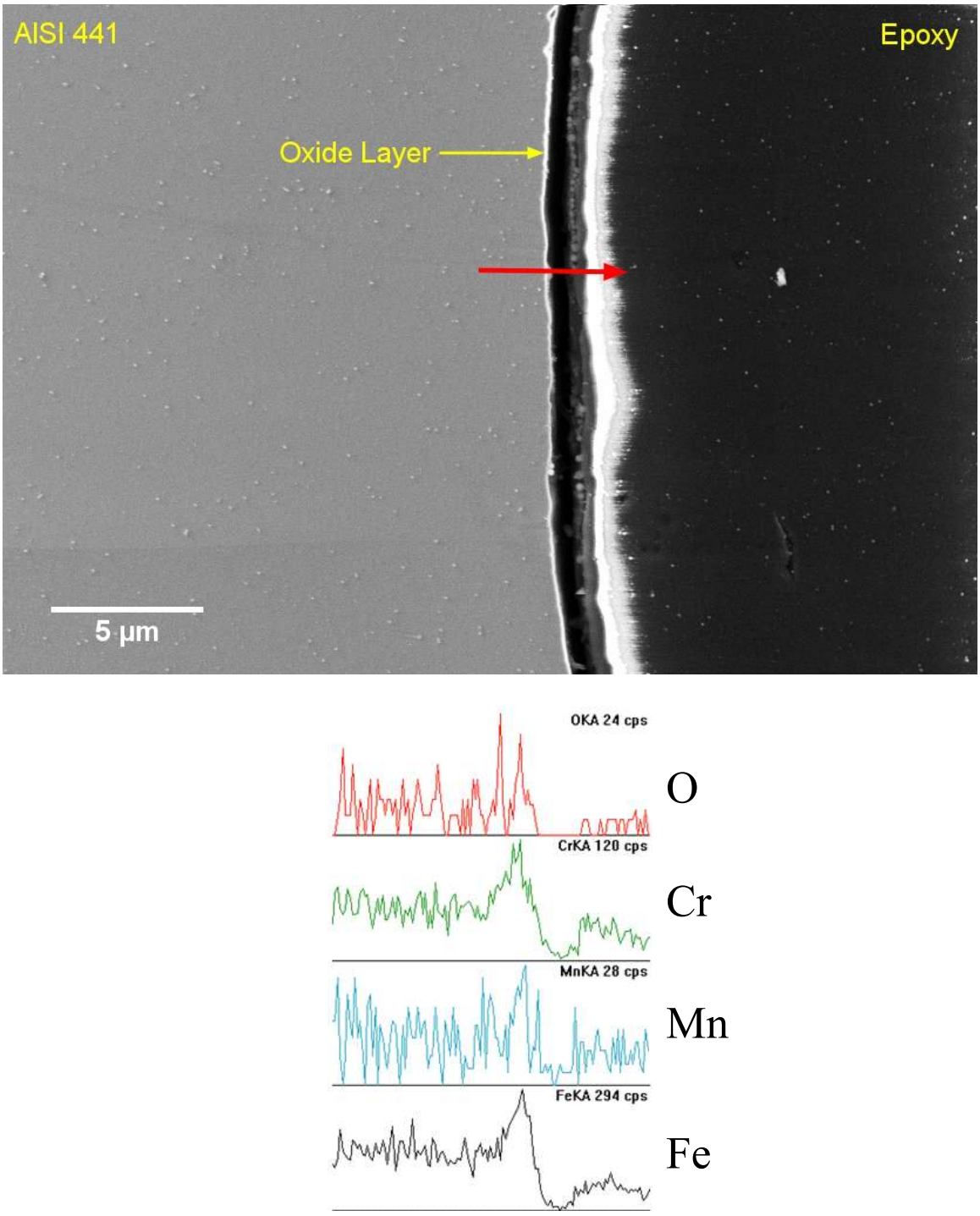

Figure 4.3.1: As-received AISI 441 oxide layer on 0.5 mm thick before exposure accompanied by EDX line scan composition.

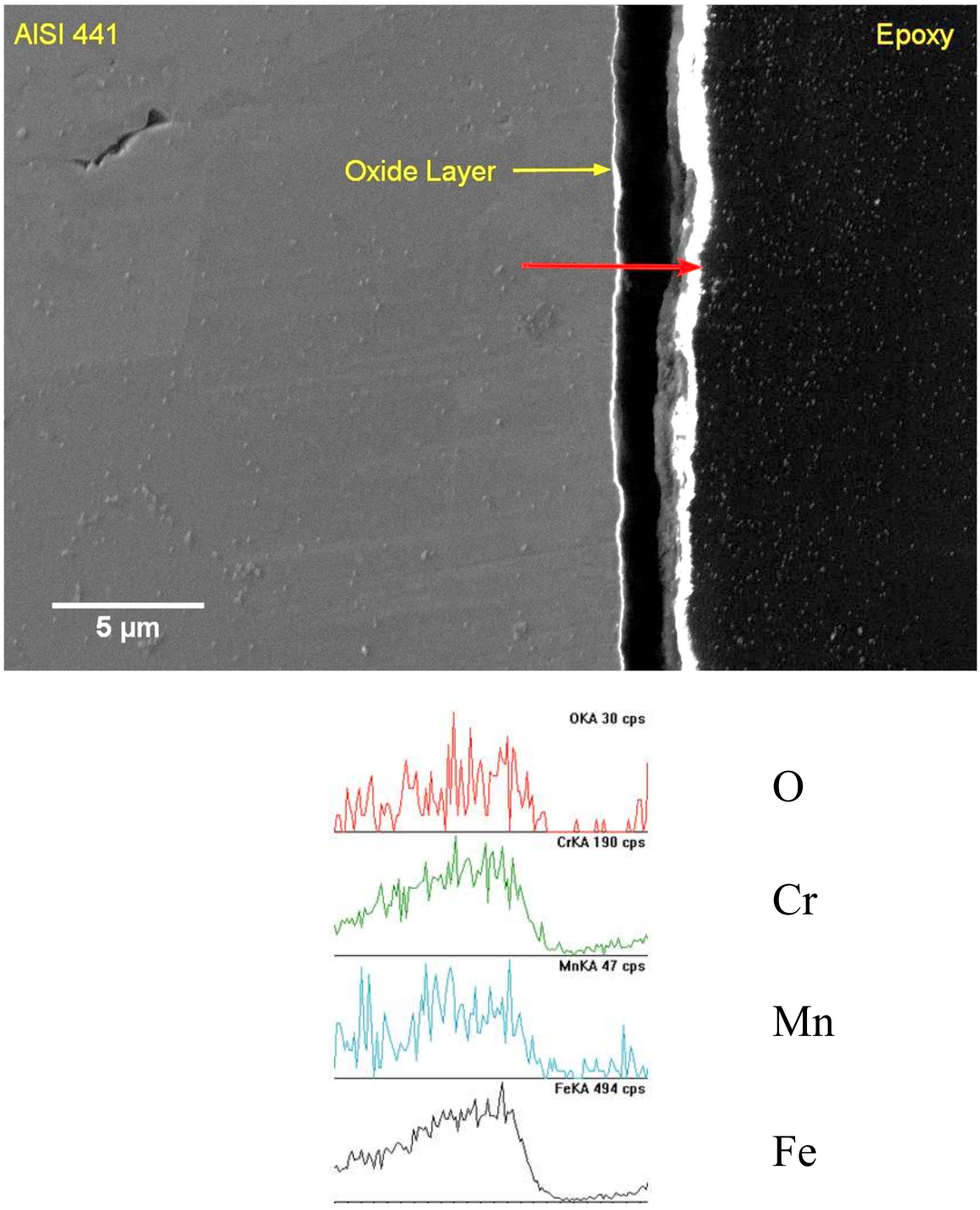

Figure 4.3.2: As-received AISI 441 oxide layer on 1.2 mm thick before exposure accompanied by EDX line scan composition.

To better establish the morphology and elemental composition of the as-received samples, the surface oxide was viewed under FE-SEM. Differences in appearance are readily observed and likely generated from manufacturing technique. EDX spot scans show the composition of the surface oxides to be chromia. If the scan is continued for any length of time, iron becomes the predominant element due to penetration of the thin oxide layer at high voltages. The below EDX scans were terminated as the iron detected by the scan began to increase.

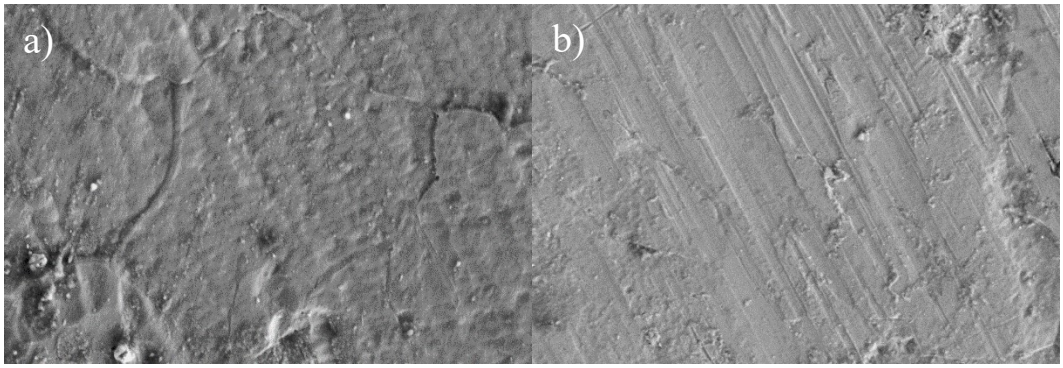

Figure 4.3.3: Surface oxides of as-received samples. a) 0.5 and b) 1.2 mm samples.

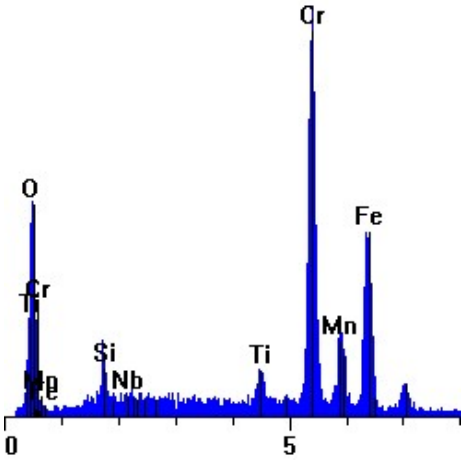

Element	Wt%	At%
O	51.13	77.40
Si	1.21	1.05
Ti	1.33	0.67
Cr	24.81	11.56
Mn	2.49	1.10
Fe	18.90	8.19
Nb	0.12	0.03

Figure 4.3.4: Surface Oxide Composition of 0.5 mm Control Sample

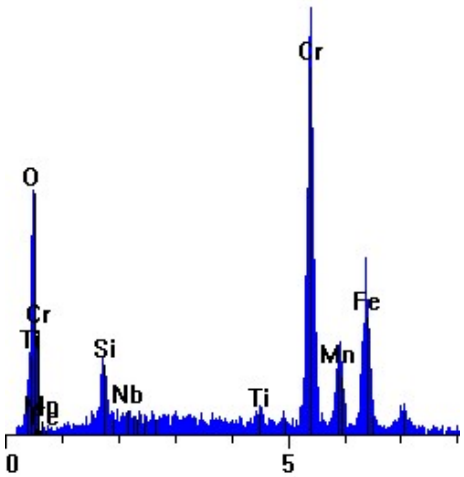

Element	Wt%	At%
O	62.87	84.44
Si	1.68	1.28
Ti	0.49	0.22
Cr	21.85	9.03
Mn	2.19	0.86
Fe	10.72	4.12
Nb	0.21	0.05

Figure 4.3.5: Surface Oxide Composition of 1.2 mm Control Sample

Single Atmosphere Exposure Oxide Evolution

The oxide scale thickness of as-received samples was found to be 0.19 and 0.11 µm for the 0.5 and 1.2 mm thick samples, respectively. These values serve as the baseline for comparison as exposure times and environment types change. In single atmosphere exposure at 800°C, both samples saw oxide thickness increase with length of exposure. Starting at 24 hours of exposure and in increments of 24 hours up to 100 hours of exposure, the average oxide thickness was seen to grow from 0.41 to 1.7 µm for the 0.5 mm sample [Table 4.3.1 & Figure 4.3.9]. Similarly, the 1.2 mm samples saw growth from 0.70 to 1.2 µm [Table 4.3.1 & Figure 4.3.13].

Table 4.3.1: Evolution of Cross-Sectional Oxide Thickness in SA Exposure over Time.

Sample Thickness (mm)	Average Oxide Thickness Over Time Under Specified Conditions (μm)				
	0 hours	24 hours	48 hours	72 hours	100 hours
0.5	0.18	0.41	0.88	1.56	1.70
1.2	0.11	0.70	0.97	1.16	1.22

The thicknesses of the samples did not appear to impact the development of oxide scale in the single atmosphere tests. Chromium and manganese oxides ($(Cr,Mn)_2O_3$) are the major components as stated by previous studies. The elemental constituents of the oxide as determined with EDX techniques appears to agree with these studies. [Figure 4.3.9 & Figure 4.3.13]. Spot analyses confirm that the oxide compositions match the expected weight percents of chromia and manganese(III) oxide. Many minor peaks exist in this oxide including Si and Fe, but the major peaks are Cr, Mn, and O. These results are comparable with previous research.

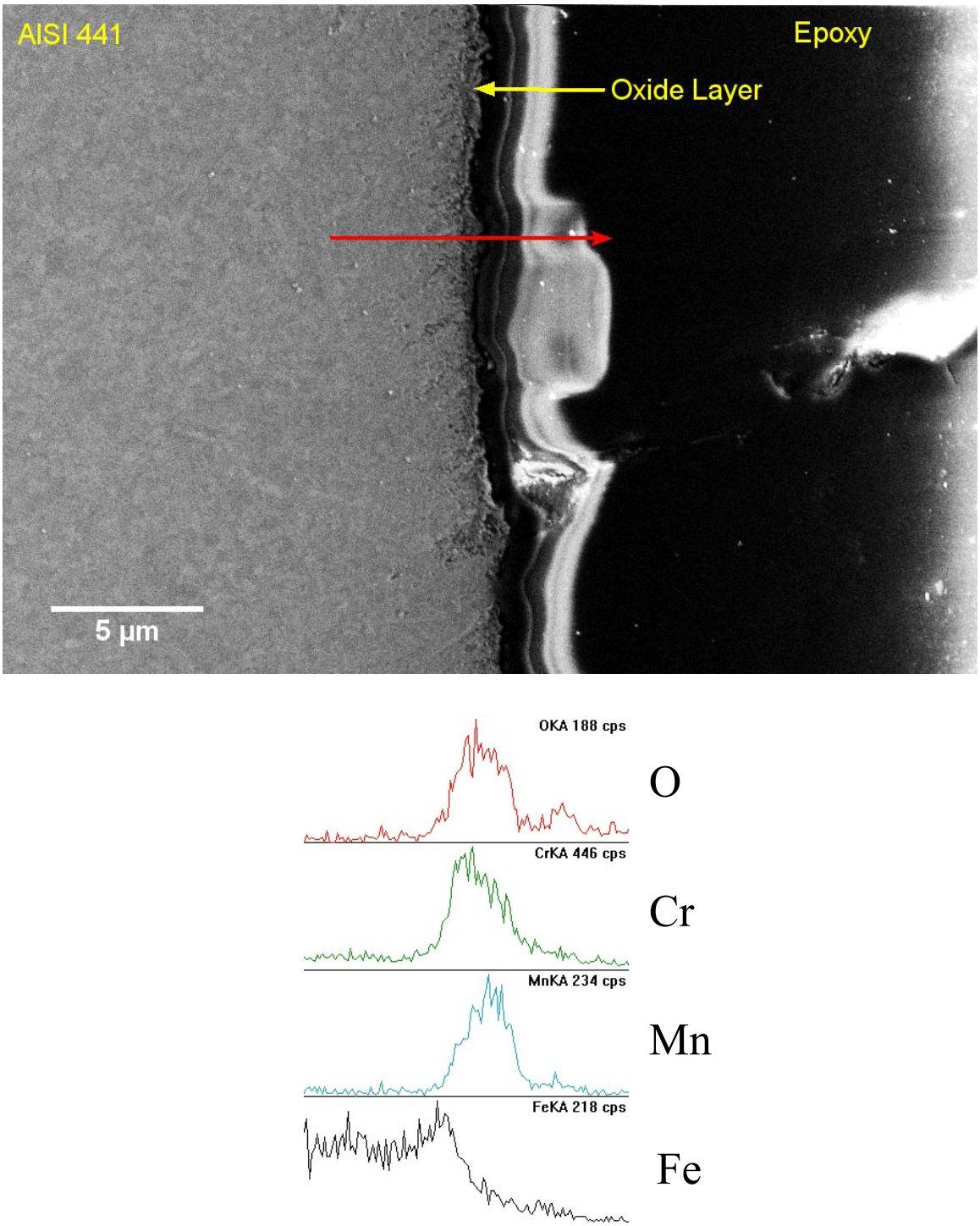

Figure 4.3.6: Development of AISI 441 oxide layer on 0.5 mm thick sample at 24 hours under single atmosphere exposure accompanied by EDX line scan composition.

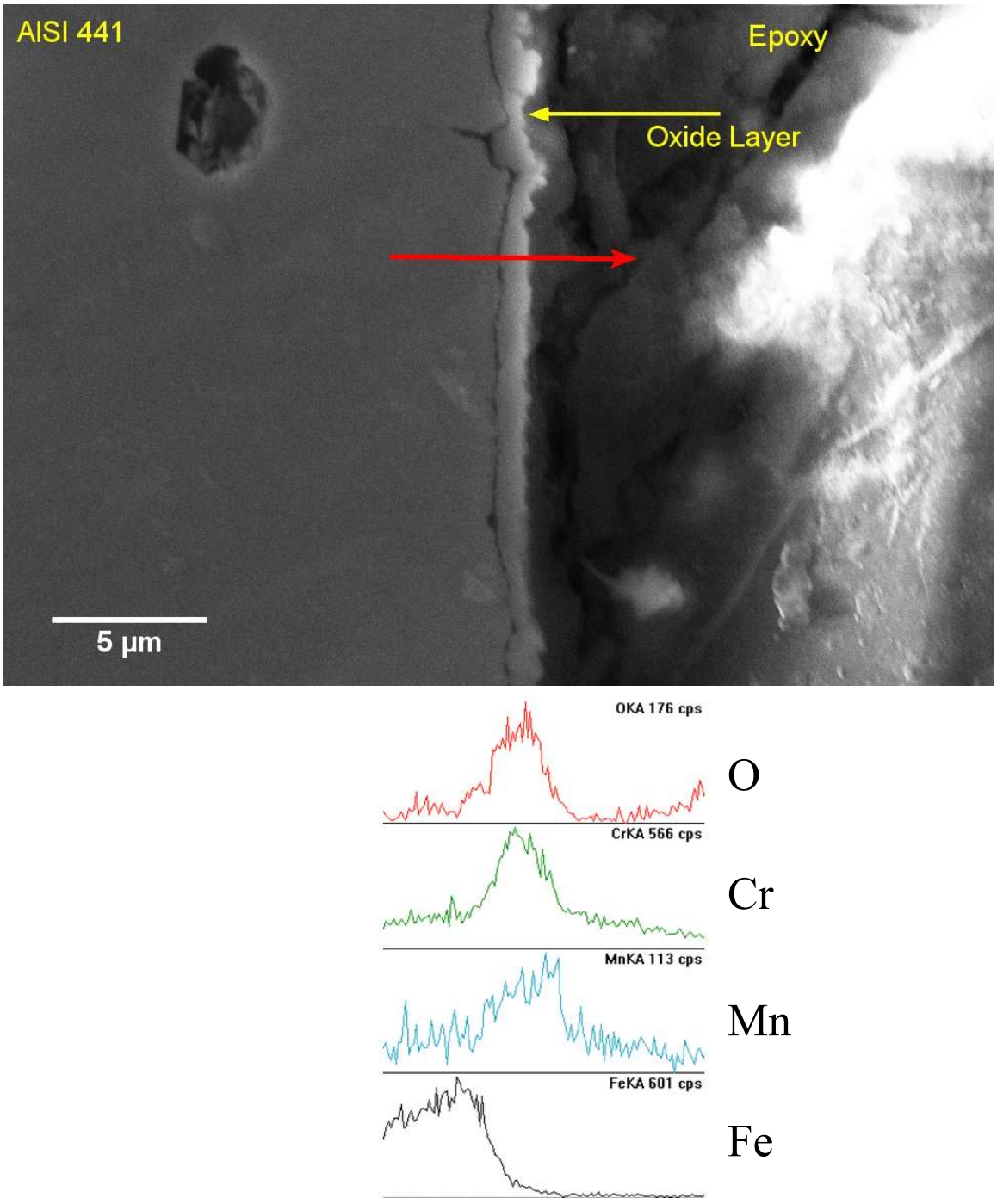

Figure 4.3.7: Development of AISI 441 oxide layer on 0.5 mm thick sample at 48 hours under single atmosphere exposure accompanied by EDX line scan composition.

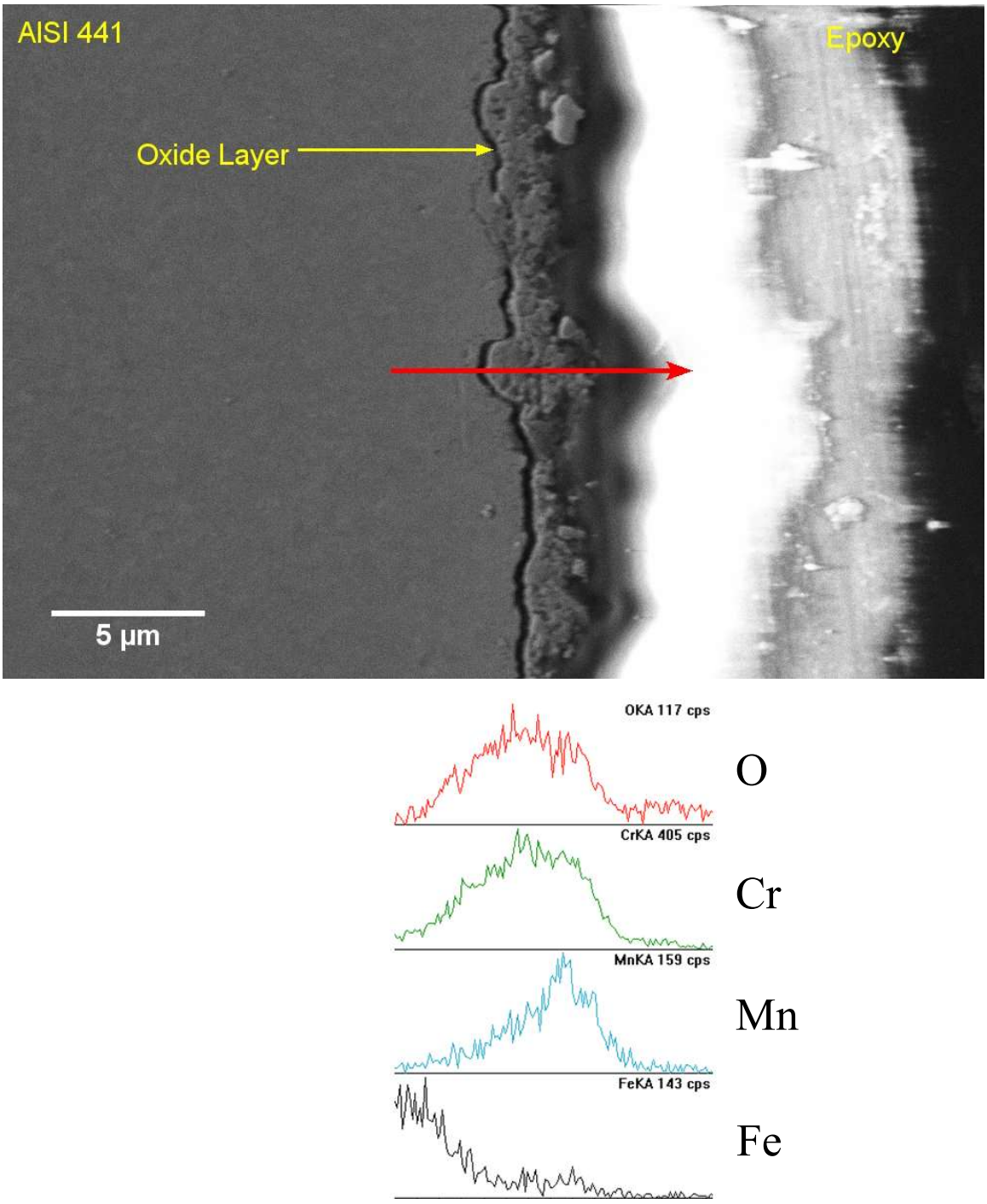

Figure 4.3.8: Development of AISI 441 oxide layer on 0.5 mm thick sample at 72 hours under single atmosphere exposure accompanied by EDX line scan composition.

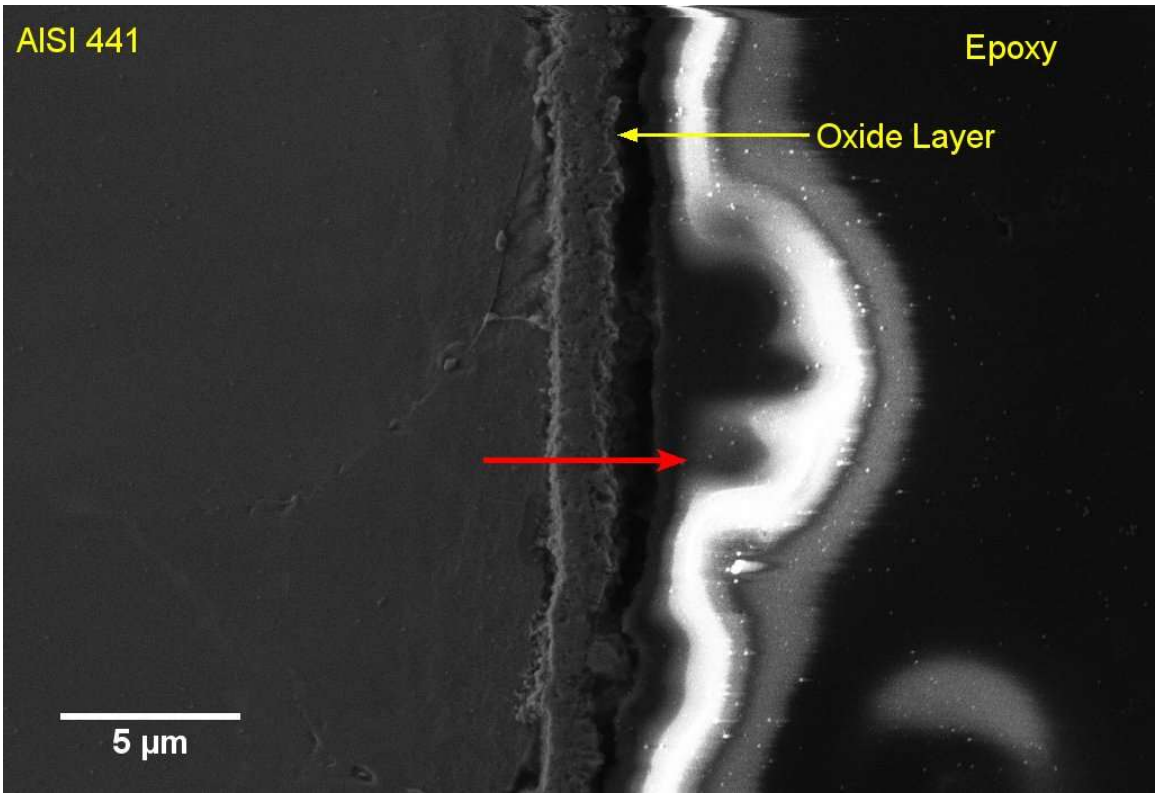

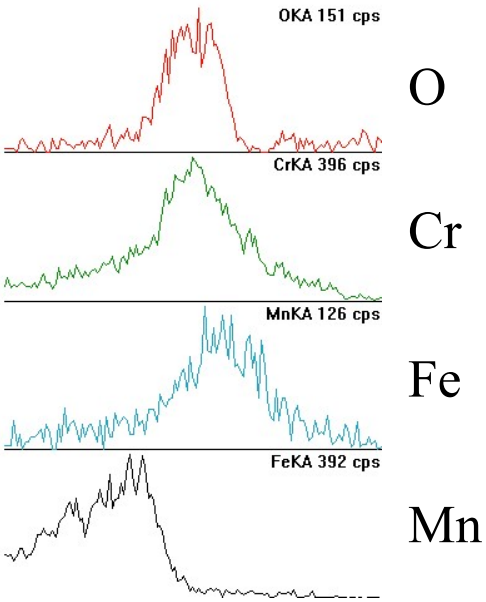

Figure 4.3.9: Development of AISI 441 oxide layer on 0.5 mm thick sample at 100 hours under single atmosphere exposure accompanied by EDX line scan composition.

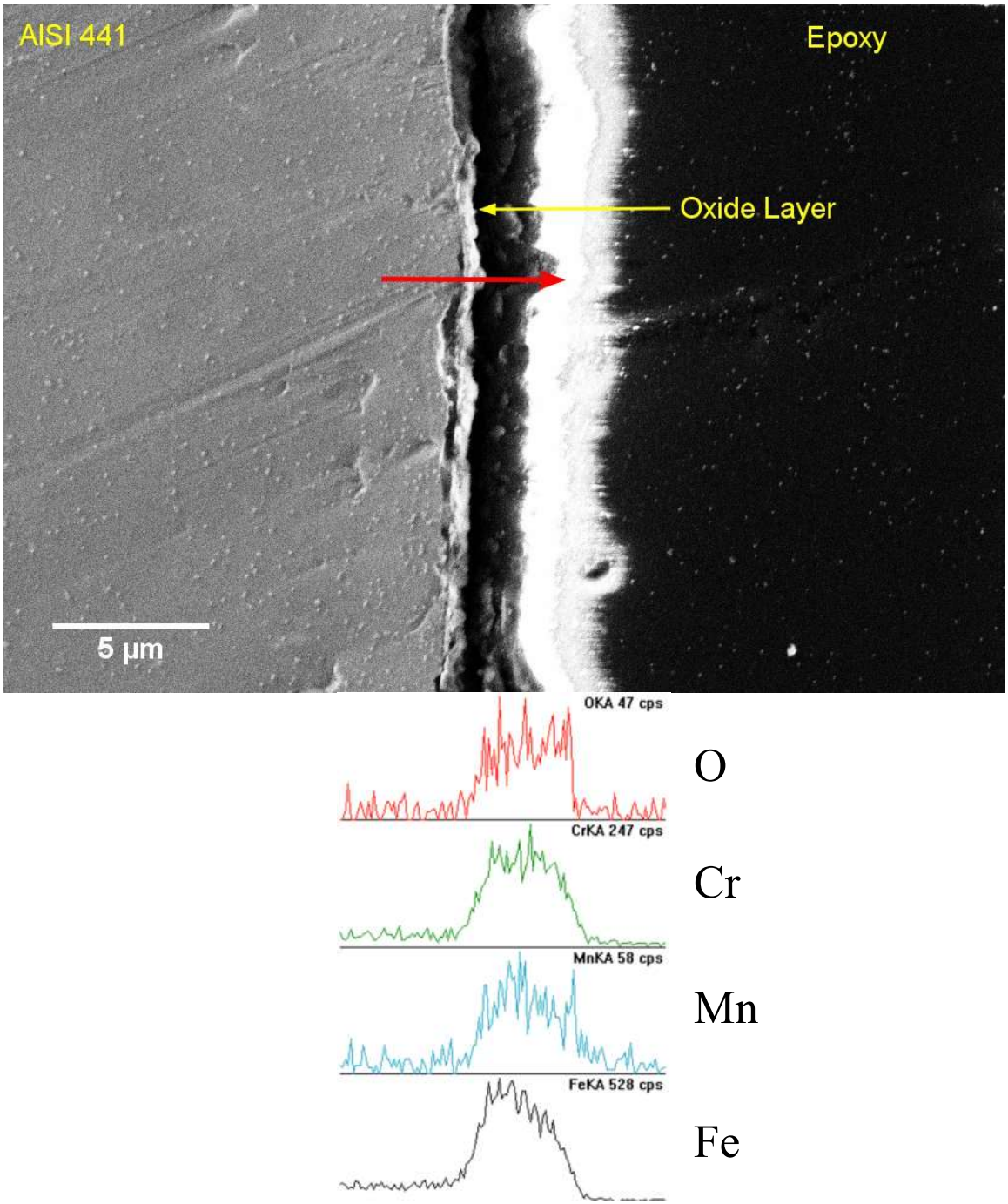

Figure 4.3.10: Development of AISI 441 oxide layer on 1.2 mm thick sample at 24 hours under single atmosphere exposure accompanied by EDX line scan composition.

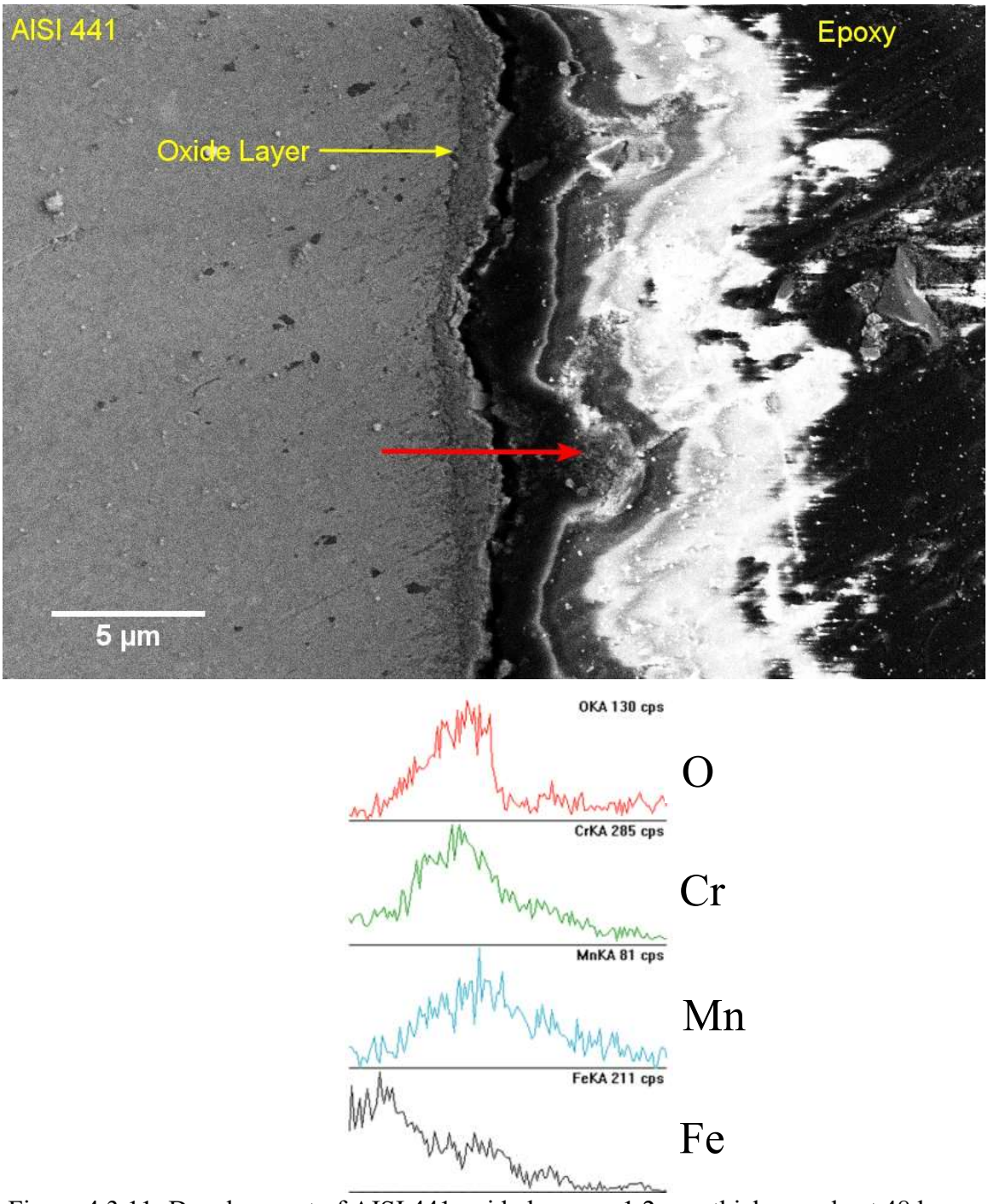

Figure 4.3.11: Development of AISI 441 oxide layer on 1.2 mm thick sample at 48 hours under single atmosphere exposure accompanied by EDX line scan composition.

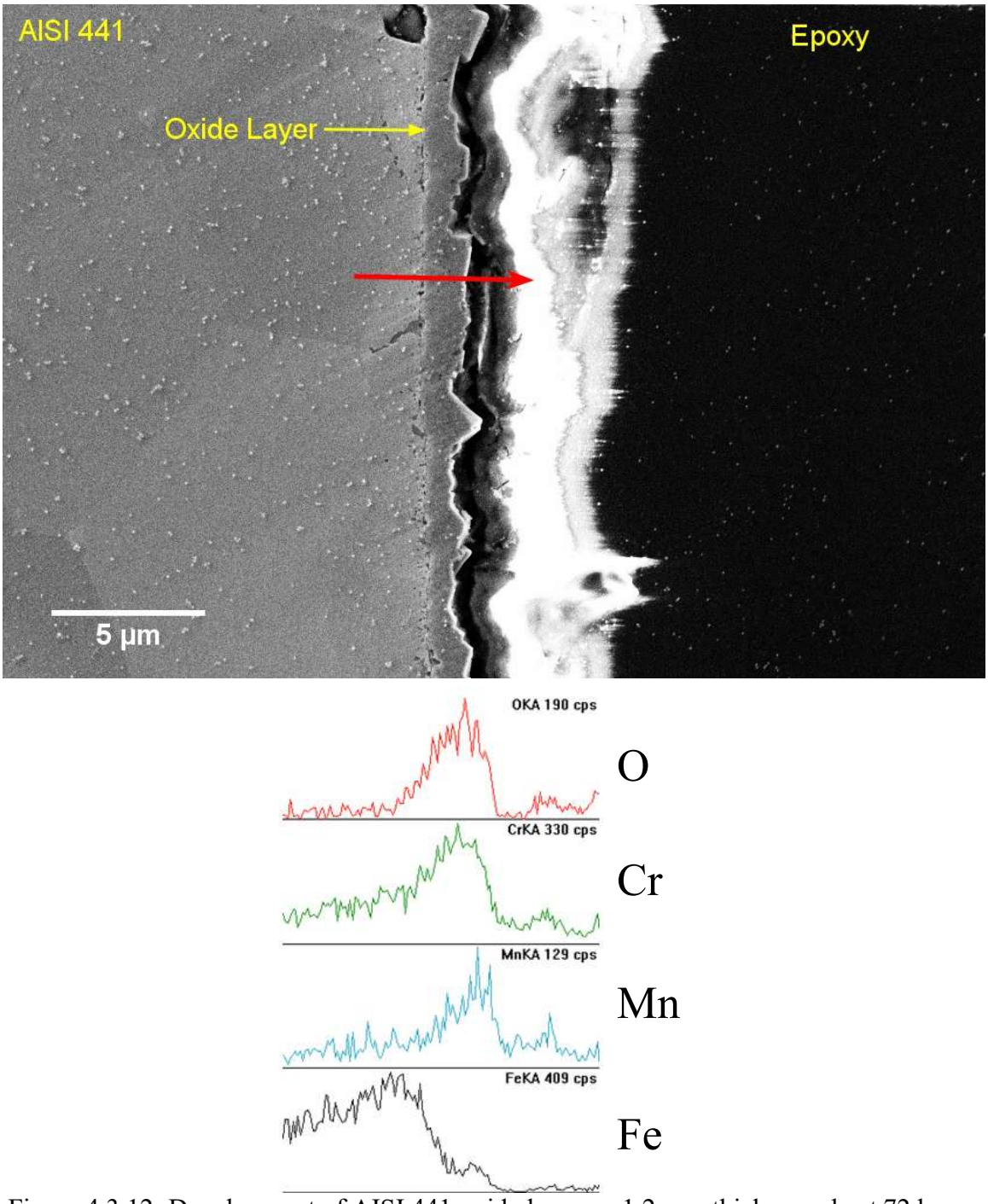

Figure 4.3.12: Development of AISI 441 oxide layer on 1.2 mm thick sample at 72 hours under single atmosphere exposure accompanied by EDX line scan composition.

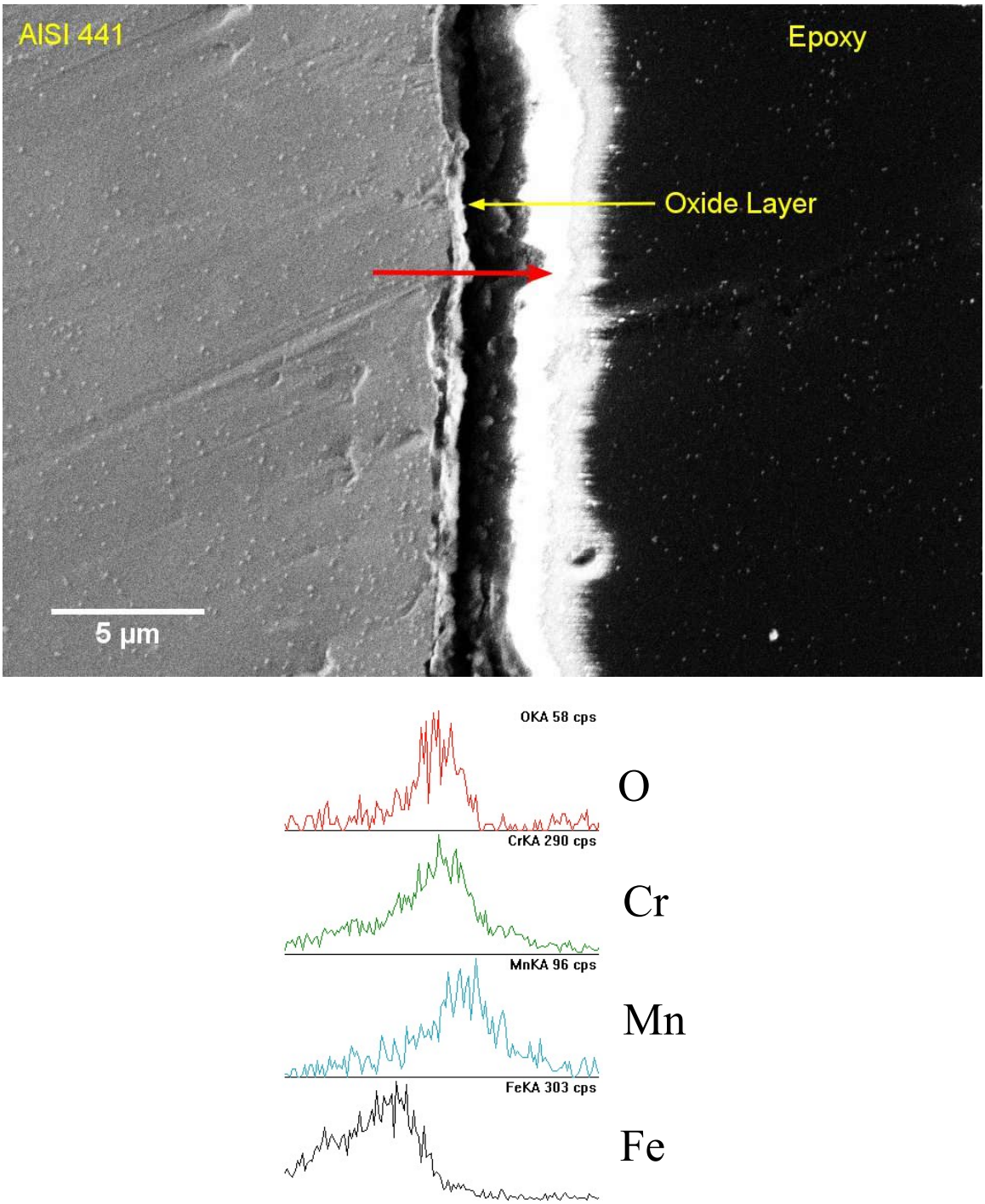

Figure 4.3.13: Development of AISI 441 oxide layer on 1.2 mm thick sample at 100 hours under single atmosphere exposure accompanied by EDX line scan composition.

Dual Atmosphere Exposure Oxide Evolution

In dual atmosphere exposure at 800°C, the 0.5 samples saw an increase in oxide thickness from 0.63 µm at 24 hours to 2.8µm at 100 hours; the 1.2 mm samples saw growth from 0.75 µm to 1.9 µm [Table 4.3.2, Figure 4.3.18, & Figure 4.3.23]. In all cases observed, the average thickness of the oxide increased with increase in time of exposure as expected from previous research. The thicknesses of the samples appeared to play little role in the development of the oxide as in the single atmosphere tests.

The oxide thickness for the dry DA and 5%H-95%Ar exposure tests are shown on this table as well; please note, only a 100 hour experiment was performed with these environments and images of these oxide cross-sections are not presented here. The oxide thicknesses of these environments are similar to, yet consistently less than, the DA exposure for 100 hours. For the 0.5 mm thick samples, the oxide thicknesses of the dry DA and PP DA exposures are 1.37 µm and 1.40 µm, respectively. For the 1.2 mm samples, the thicknesses after exposure are 1.60 and 1.14 µm.

Table 4.3.2: Evolution of Cross-Sectional Oxide Thickness in SA Exposure over Time.

Sample Thickness (mm)	Environmental Exposure	Average Oxide Thickness Over Time Under Specified Conditions (µm)				
		0 hours	24 hours	48 hours	72 hours	100 hours
0.5	DA	0.19	0.63	0.70	1.70	2.76
	Dry DA		--	--	--	1.37
	PP DA (5% H)		--	--	--	1.40
1.2	DA	0.11	0.75	1.18	1.30	1.88
	Dry DA		--	--	--	1.60
	PP DA (5% H)		--	--	--	1.14

The oxide scale seen in dual atmosphere tests shows that two layers of oxide exist. Similar to the SA case, manganese and chromium oxides ($(Cr,Mn)_2O_3$) comprise the majority of the sublayer as seen by the spot scan via EDX techniques [Figure 4.3.14]. As with SA exposure, the iron percentage drops drastically as the oxide begins. In DA exposure, however, iron content increases the top layer of oxidation. The top oxide is a hematite ($Fe_2O_{3)}$ oxide that limits the use of AISI 441 as SOFC interconnects due to its poor electrical performance. An EDX spot scan of the outer oxide on the 1.2mm, 24 hour DA exposure sample confirms this composition [Figure 4.3.15]. Both layers continue to grow with time, however, the hematite layer grows more quickly.

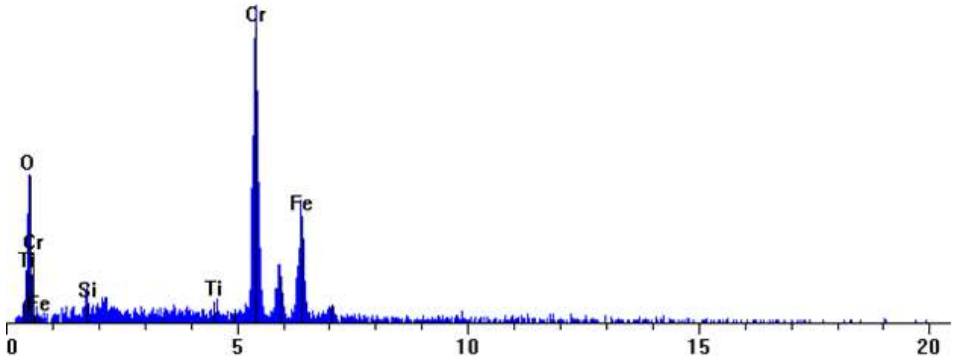

Element	KRatio	Wt%	At%	ChiSquared	Z Corr	A Corr	F Corr
O	0.3348	40.62	69.14	1.16	0.893	1.644	1.000
Si	0.0075	0.96	0.94	0.93	0.956	1.624	0.999
Ti	0.0095	0.75	0.43		1.080	1.006	0.883
Cr	0.4442	38.35	20.09	3.10	1.087	0.996	0.965
Fe	0.2040	19.31	9.42	0.87	1.090	1.050	1.000
Total	**1.0000**	**100.00**	**100.00**	**0.19**			

Figure 4.3.14: EDX spot scan of inner oxide on DA sample

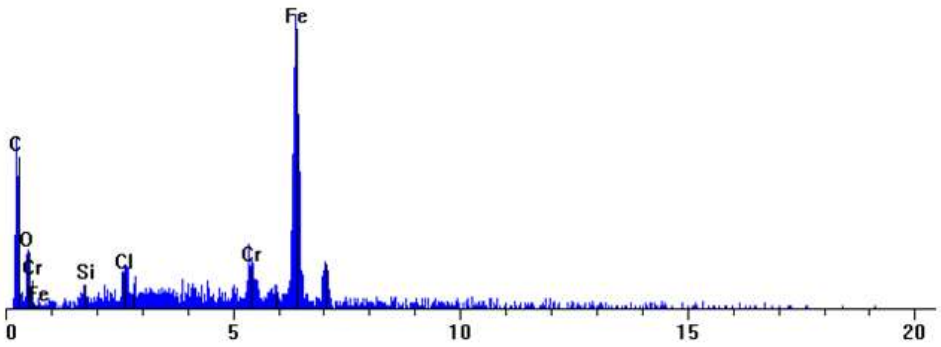

Element	KRatio	Wt%	At%	ChiSquared	Z Corr	A Corr	F Corr
C	0.1978	34.84	57.16	4.52	0.910	3.430	0.999
O	0.1240	22.23	27.38	2.35	0.931	3.416	0.999
Si	0.0020	0.17	0.12		0.992	1.477	0.999
Cl	0.0148	0.97	0.54	0.92	1.048	1.107	0.995
Cr	0.0409	2.18	0.83	0.26	1.134	0.991	0.841
Fe	0.6205	39.61	13.97	0.71	1.140	0.992	1.000
Total	**1.0000**	**100.00**	**100.00**	**0.09**			

Figure 4.3.15: EDX spot scan of outer oxide on DA sample

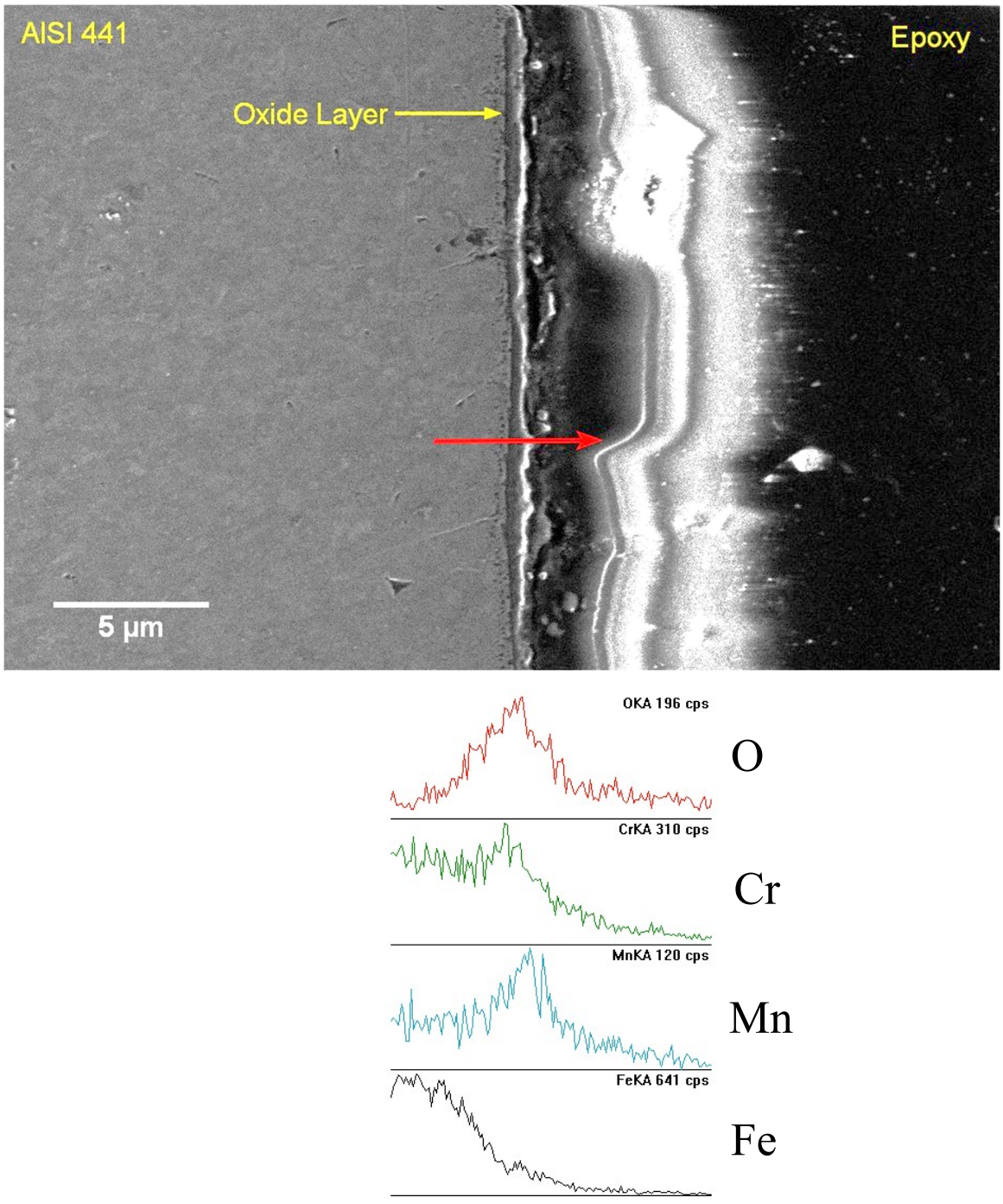

Figure 4.3.16: Development of AISI 441 oxide layer on 0.5 mm thick sample at 24 hours under dual atmosphere exposure accompanied by EDX line scan composition.

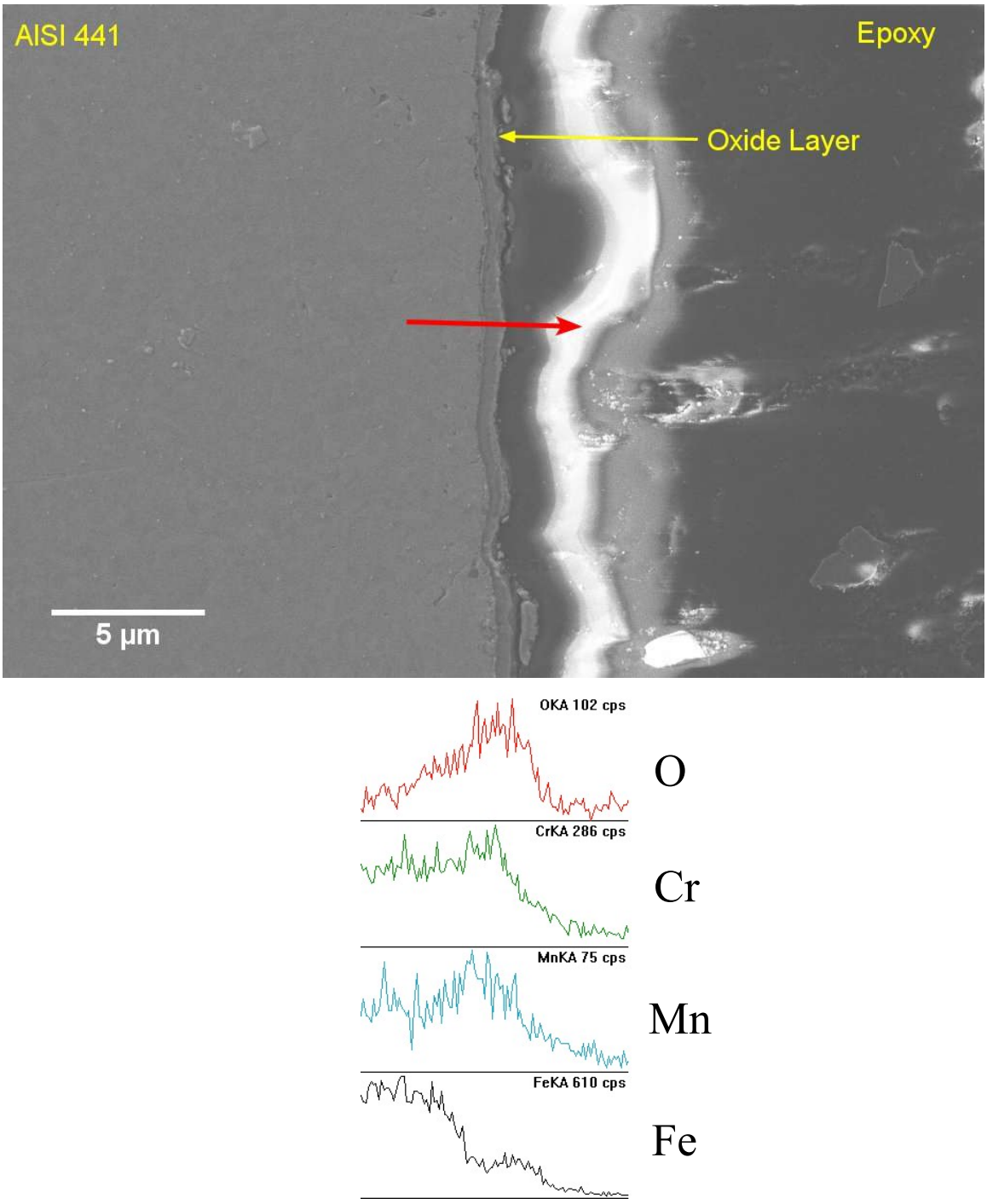

Figure 4.3.17: Development of AISI 441 oxide layer on 0.5 mm thick sample at 48 hours under dual atmosphere exposure accompanied by EDX line scan composition.

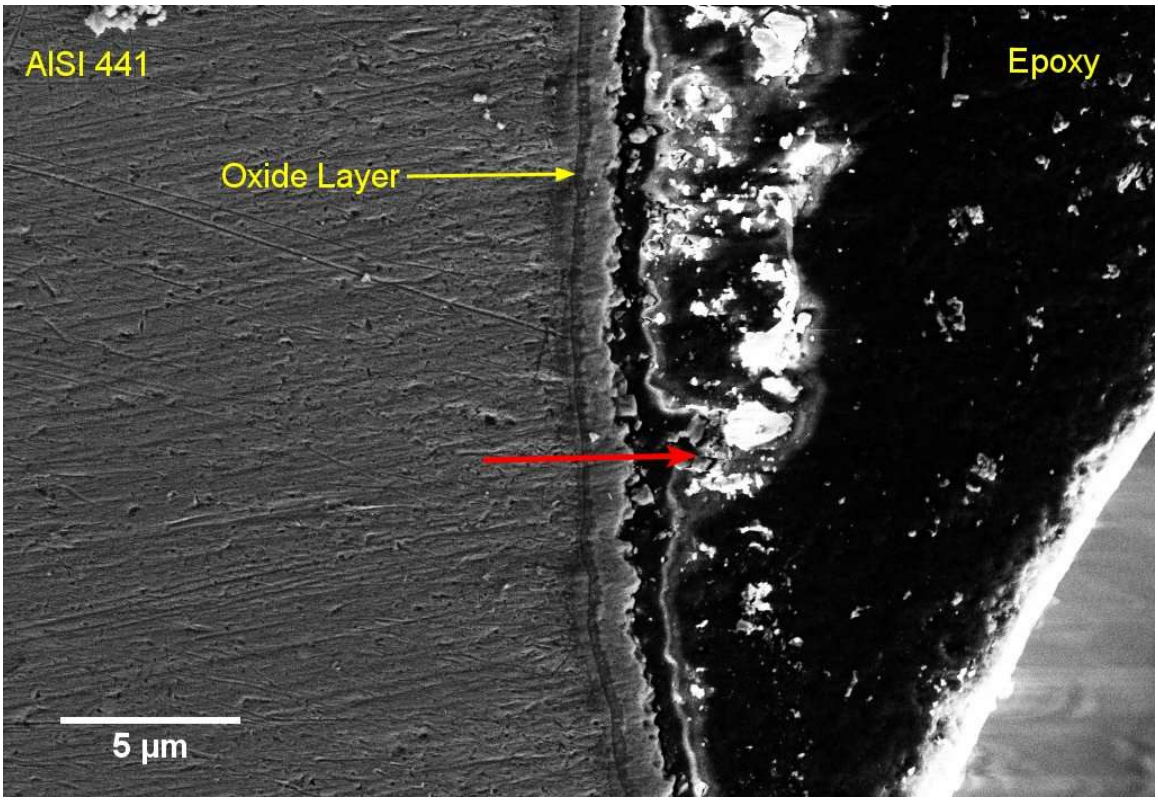

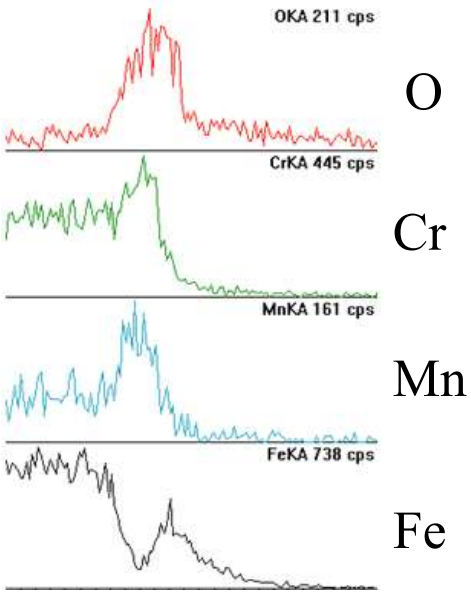

Figure 4.3.18: Development of AISI 441 oxide layer on 0.5 mm thick sample at 72 hours under dual atmosphere exposure accompanied by EDX line scan composition.

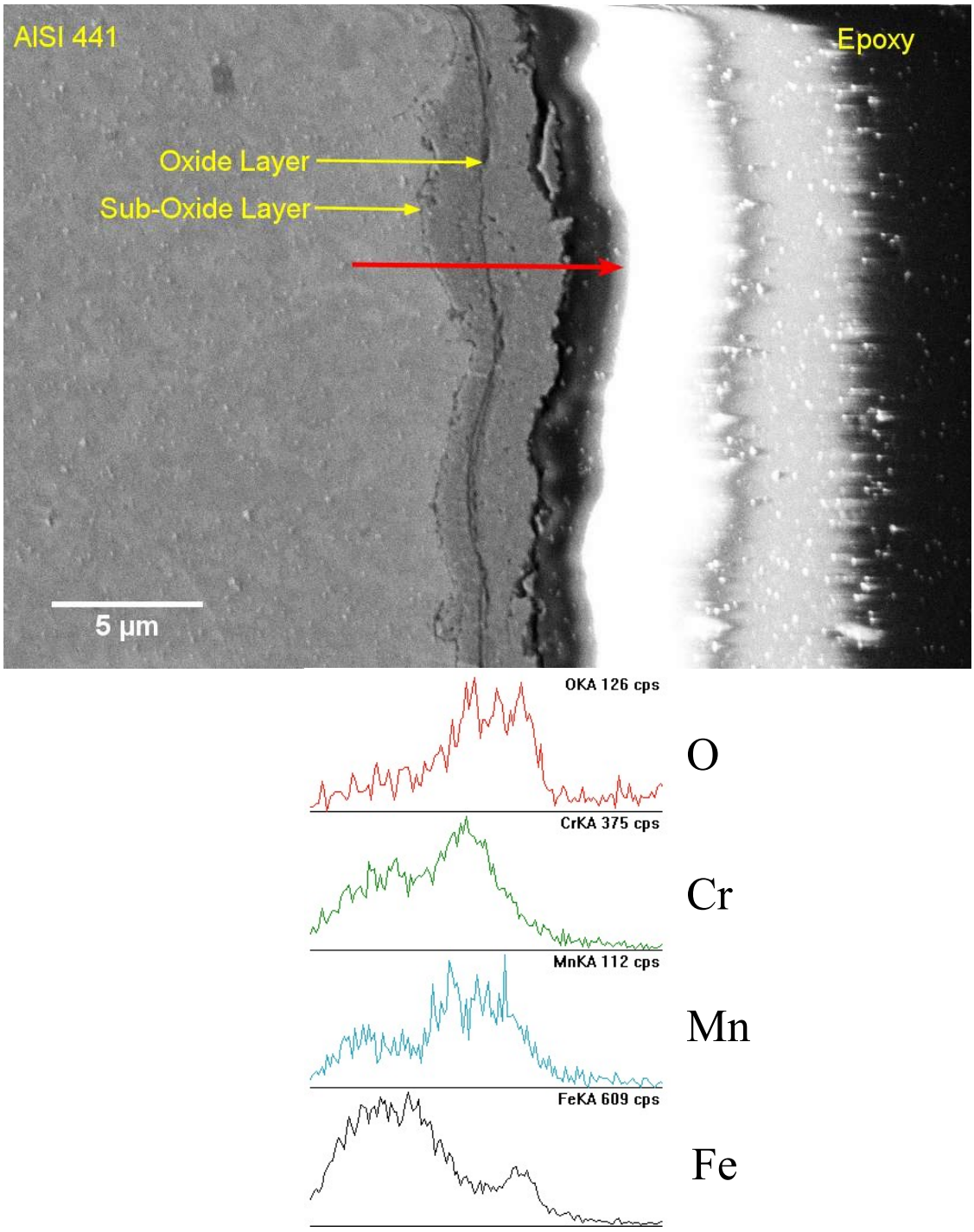

Figure 4.3.19: Development of AISI 441 oxide layer on 0.5 mm thick sample at 100 hours under dual atmosphere exposure accompanied by EDX line scan composition.

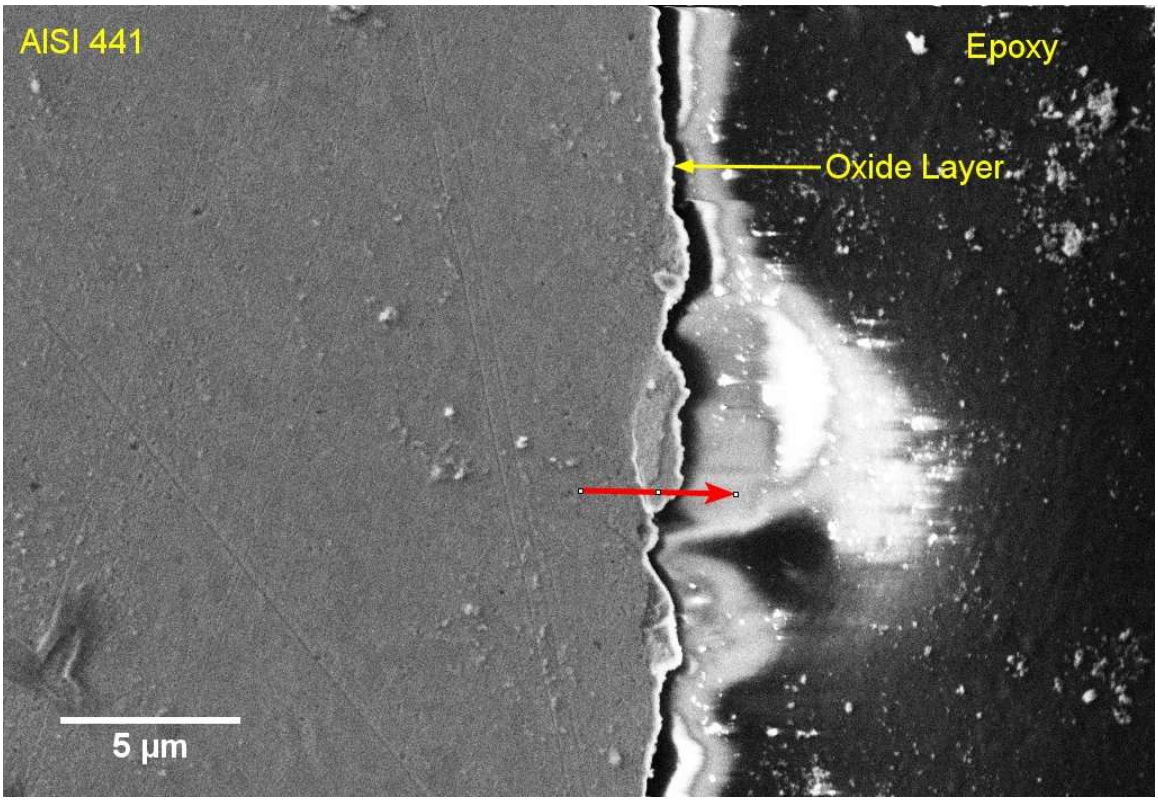

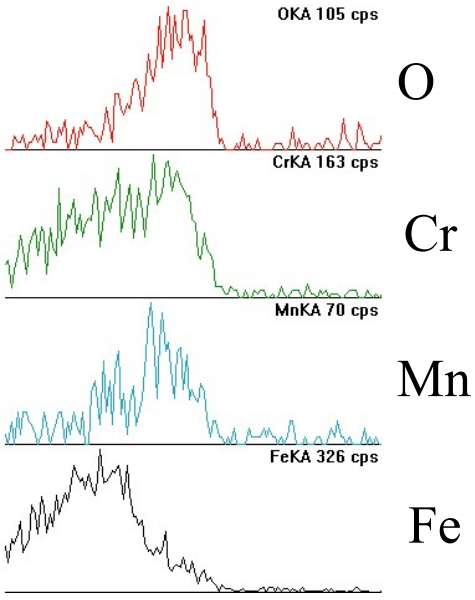

Figure 4.3.20: Development of AISI 441 oxide layer on 1.2 mm thick sample at 24 hours under dual atmosphere exposure accompanied by EDX line scan composition.

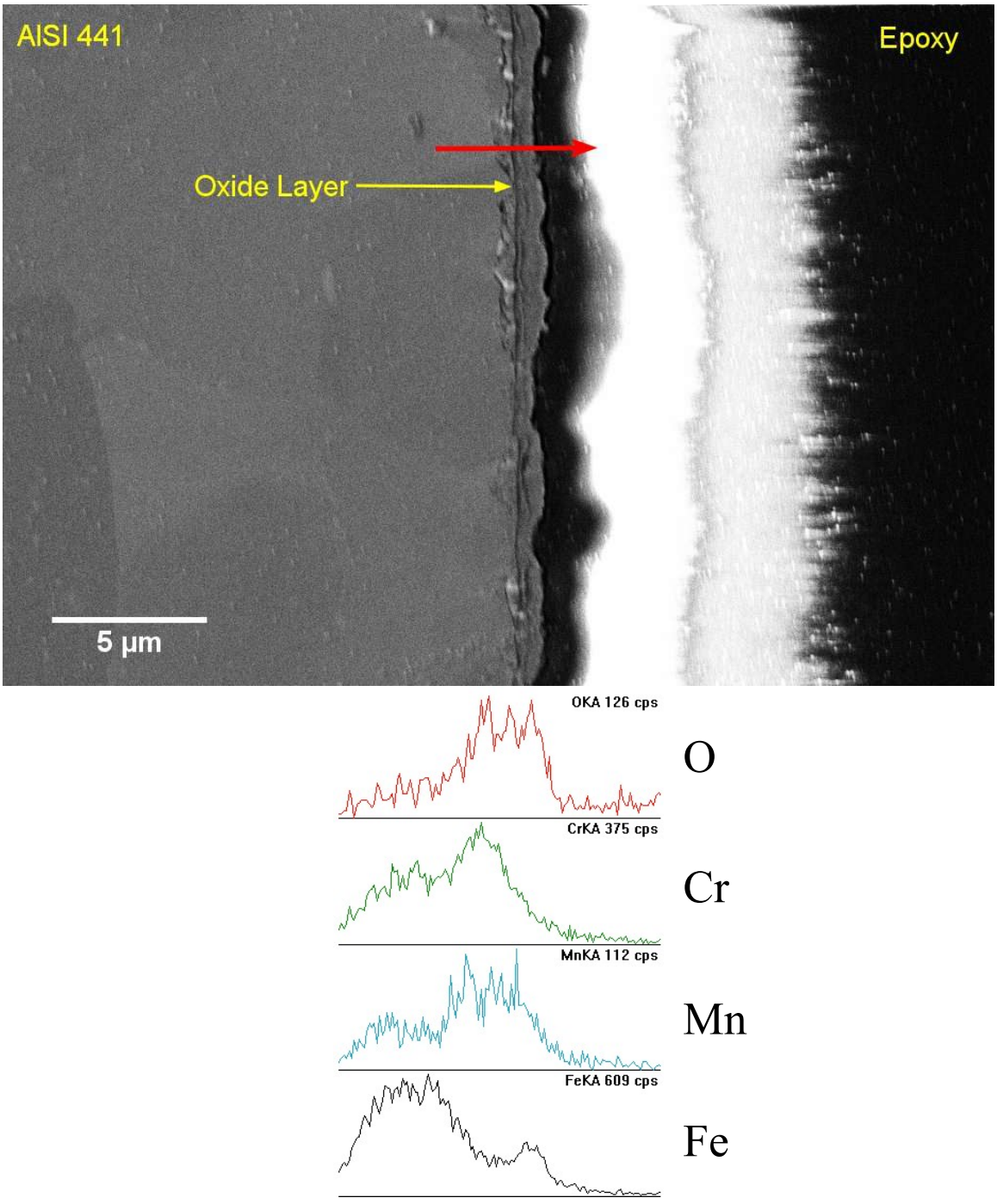

Figure 4.3.21: Development of AISI 441 oxide layer on 1.2 mm thick sample at 48 hours under dual atmosphere exposure accompanied by EDX line scan composition.

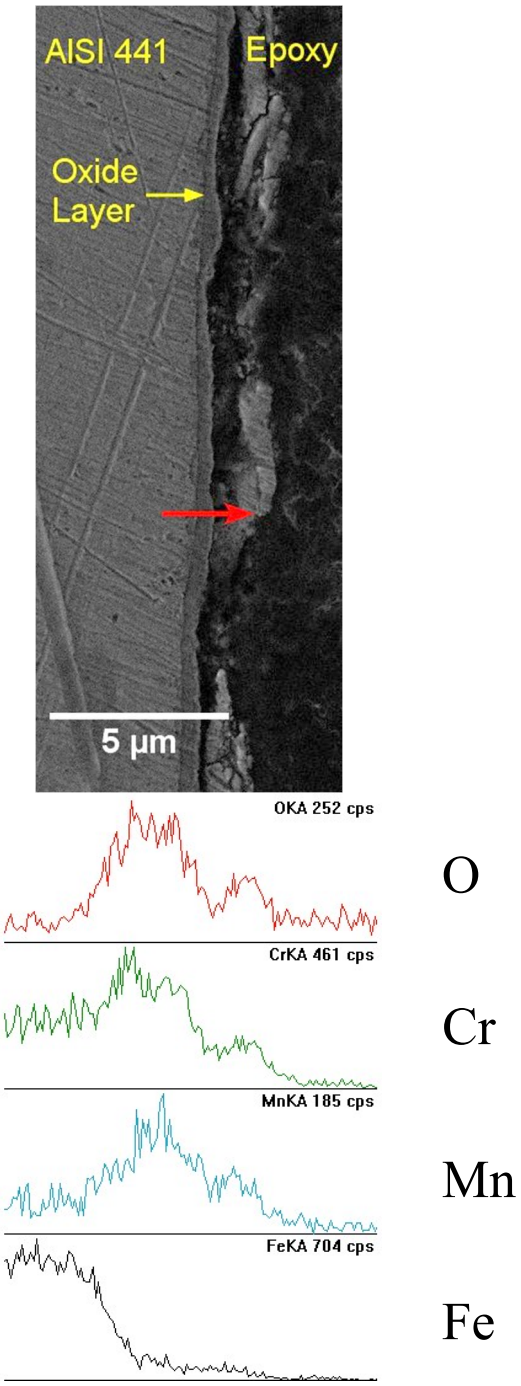

Figure 4.3.22: Development of AISI 441 oxide layer on 1.2 mm thick sample at 72 hours under dual atmosphere exposure accompanied by EDX line scan composition.

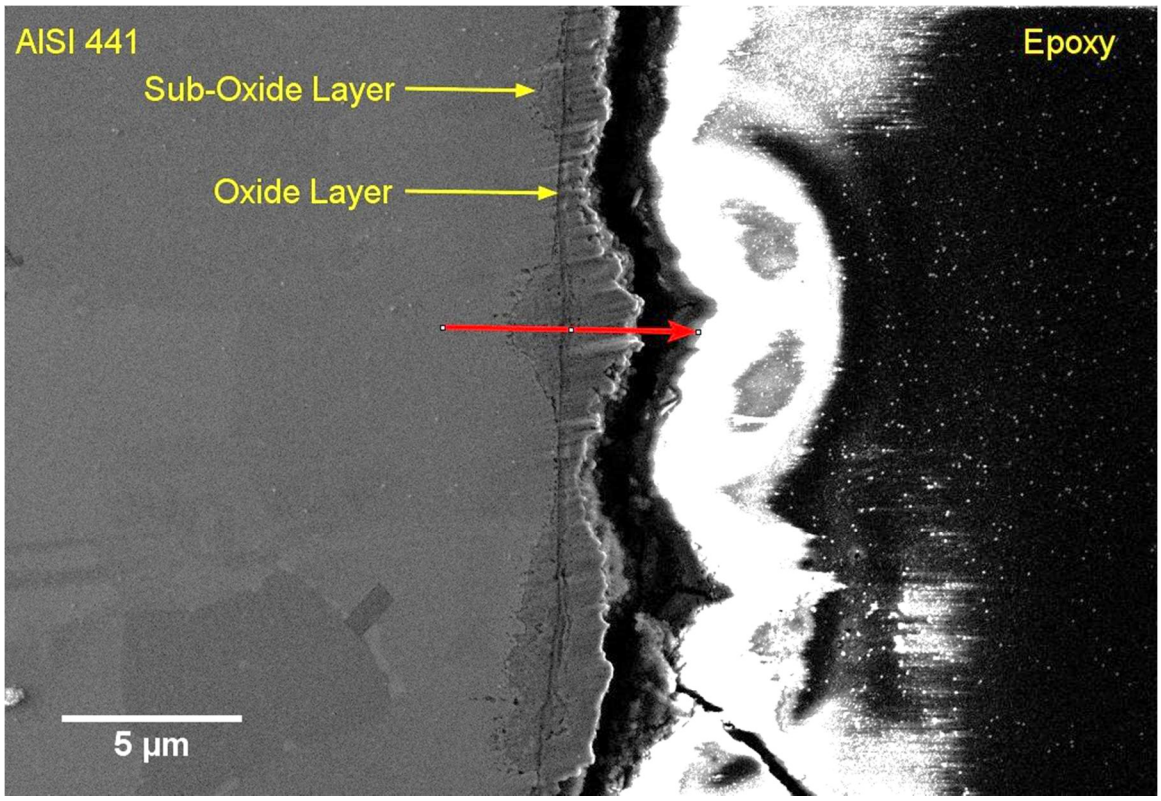

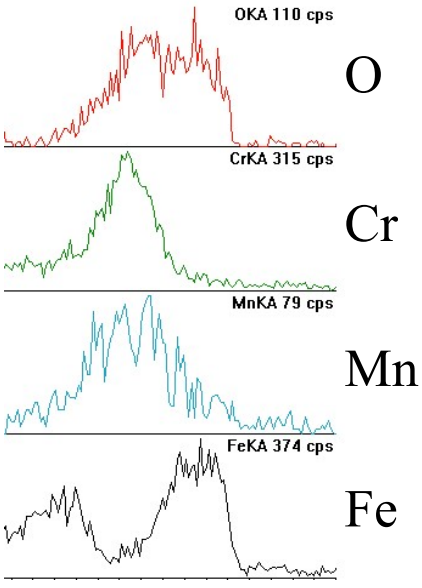

Figure 4.3.23: Development of AISI 441 oxide layer on 1.2 mm thick sample at 100 hours under dual atmosphere exposure accompanied by EDX line scan composition.

Vacuum Furnace Heat
Treatment Oxide Evolution

The surface oxide did not see growth after 100 hours in the vacuum chamber. The oxide thickness was seen to be 0.20 μm on the 0.5 mm thick sample, very similar to the 0.19 μm of the control sample. On the 1.2 mm thick coupon, the oxide thickness was seen to be 0.16 μm; the control sample oxide thickness was 0.11 μm. This is comparable to the control samples as oxidation cannot occur in the absence of oxygen in the environment.

Table 4.3.3: Cross-Sectional Oxide Thickness after Vacuum Furnace Testing

Sample Thickness (mm)	Environmental Exposure	Average Oxide Thickness (μm)	
		0 hours	100 hours
0.5	Vacuum	0.19	0.20
1.2	Vacuum	0.11	0.16

Progression of Oxide
Scale Growth over Time

It is well known that surface oxides see anomalous and accelerated growth when exposed to dual atmosphere conditions (23; 24; 25). In order to characterize the evolution of the Laves phase with regards to its effects on hydrogen transport and subsequent oxide growth, it is essential to track oxide growth throughout the same tests. The mechanisms of the accelerated oxidation are not completely understood, however, the leading explanation is that hydrogen fills interstitial sites within the metal matrix, generating a localized charge imbalance. This imbalance then encourages the oxygen ions to diffuse

into the metal and interact with the alloy (29). For AISI 441, the common reactions are the formation of hematite and chromia oxides.

In the case of all samples of this test, the oxide thickness increased over time. In the 0.5 mm sample tests in single atmosphere, the oxide thickness appears to grow linearly over these time frames at a rate of approximately 0.016 μm / hour [Figure 4.3.24]. Contrarily, the 1.2 mm SA samples sees an initial jump in oxide thickness from 0.1 μm to 0.75 μm over the first 24 hours, showing an oxide growth at a rate of 0.027 μm / hour [Figure 4.3.25]. After this time frame, the oxide layer develops at a slower rate of 0.007 μm / hour.

The dual atmosphere samples do not follow the same trend of linear growth. In the early stages of dual atmosphere exposure, the oxide grows at a similar rate to the single atmosphere examples before taking off in a decidedly non-linear trend. While in the first couple days of exposure the oxide scale development is similar to the SA case, as the exposure time to DA increases, the oxidation thickness develops at an increased rate without showing signs of slowing.

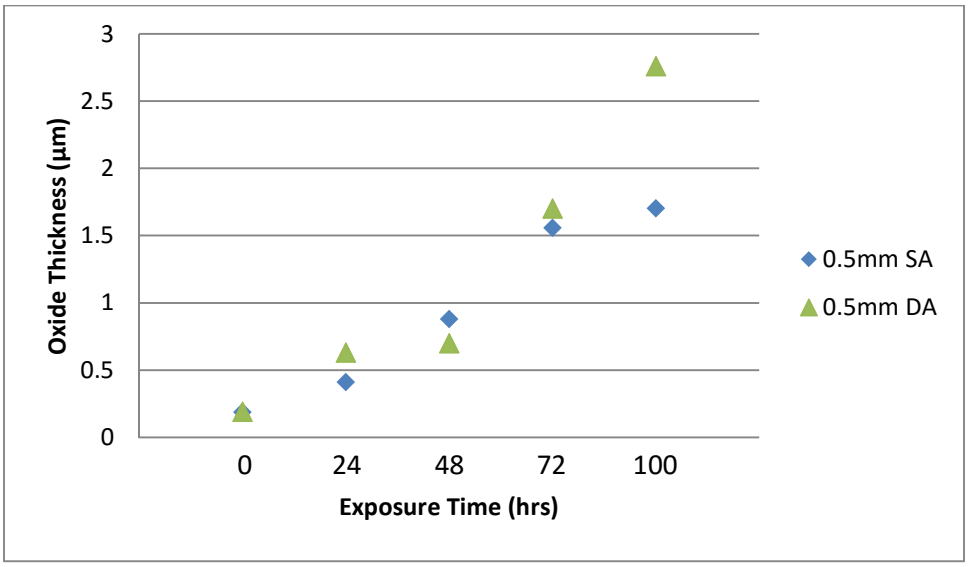

Figure 4.3.24: Oxide growth of 0.5 mm thick samples after exposure to specified times of single and dual atmosphere testing at 800°C.

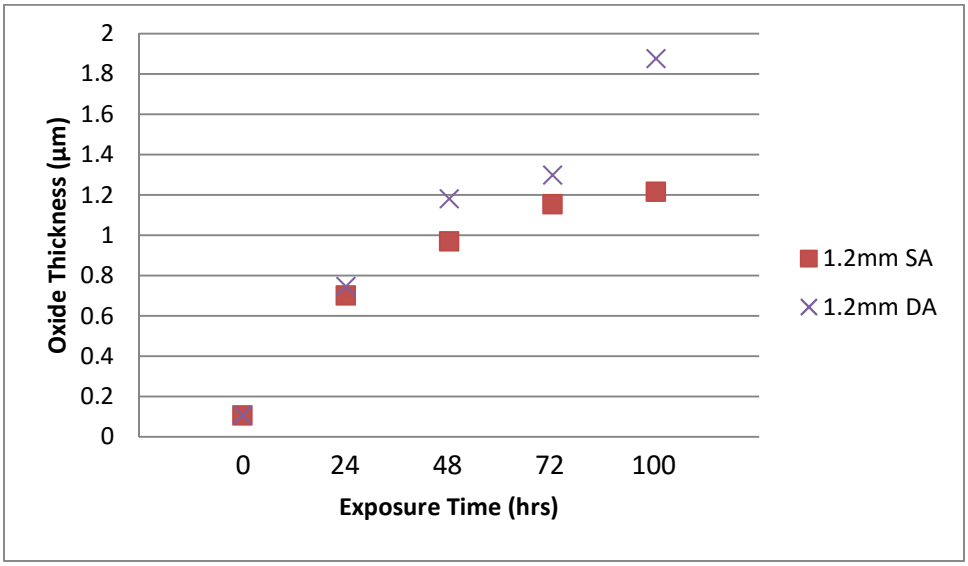

Figure 4.3.25: Oxide growth of 1.2 mm thick samples after exposure to specified times of single and dual atmosphere testing at 800°C.

Comparison of Oxide
Evolution after Environment Exposure

The main factors that varied during the testing of these samples were the moisture content and hydrogen concentrations. The bulk of this study focused on the SA and DA exposure where both test included approximately 3% H_2O and the leading difference was the introduction of a hydrogen gradient across the material thickness. In this case, it is seen that the oxide development for each sample thickness was greatly increased by the introduction of hydrogen. The most obvious difference between in oxides due to the environments is the development and growth of two oxide layers after DA exposure. The two oxide types, Fe_2O_3 and $(Cr,Mn)_2O_3$, growing at the same time with increased the oxygen diffusion lead to greatly accelerated and anomalous oxidation.

In the other DA experiments where no H_2O was present or the hydrogen content was reduced, the thickness of oxidation was similar to the oxide thickness from the SA test [Figure 4.3.26]. Two distinct oxide layers still developed under these environments, however, the thickness of each layer was noticeably thinner than on the moist DA test. A much more robust series of tests would be necessary to determine how the hydrogen gradient and moisture levels affect the oxidation of AISI 441.

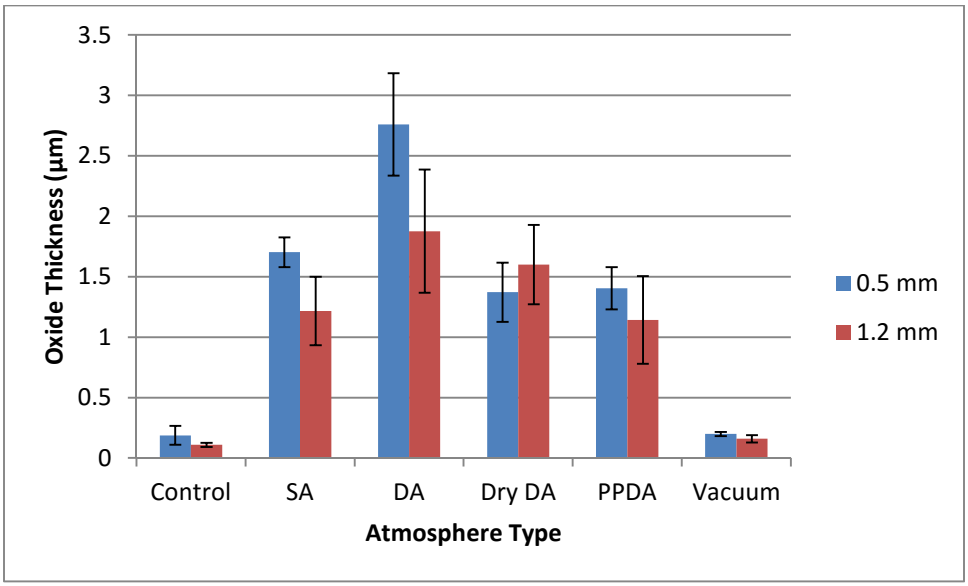

Figure 4.3.26: Oxide Thickness after 100 Hours of Exposure at 800°C to the Specified Atmosphere.

Effects of Thickness
and Grain Size on Oxidation

Many factors drive the oxidation and combine to give the final result. One major factor in this test was the thickness of compared samples. In all but the dry DA test, the 0.5 mm thick sample was seen to develop a thicker oxide than the 1.2 mm samples tested under the same conditions [Figure 4.3.26]. This suggests that the thickness of the interconnect may play a role in reduction of oxidation due to fuel cell operating conditions. That being said, the grain size and precipitates of the materials could play a major role as well.

Given the current hypothesis that the accelerated and anomalous oxidation is driven by hydrogen transport from the hydrogen-rich side to the oxygen-rich side, it goes to reason that the more efficiently the hydrogen travels through the material, the greater its effects on oxidation. The smaller grains of the 1.2 mm samples translate to more

possible pathways through the thickness of the material. The greater number of grain boundary paths would be expected to facilitate the transport of hydrogen through the material if this were the path used for transit – this is not necessarily the case, but a condition worthy of note. Despite the greater opportunity provided though, the thicker, 1.2 mm samples saw a lower rate of oxidation than the 0.5 mm samples, thereby suggesting either the grain boundaries are not the path of transit or other factors are at work.

Another possible factor in hydrogen transport could be the precipitates that form throughout AISI 441. From the two sample thicknesses tested, the 0.5 mm thick sample had a much greater number of Laves phase precipitates along the grain boundary than was seen with the 1.2 mm thick sample, creating a much more uniform path through the material. The reason for the increased precipitation at the grain boundary for one sample and not the other is unclear, but it may facilitate hydrogen transportation through the sample as Laves phase is known to absorb hydrogen by means of interstitial sites. With a constant hydrogen gradient through the metal, these precipitates could act as reservoirs and create a path through the material that would otherwise be much more difficult to pass through.

A much greater degree of research on the topic of thickness and grain effects on hydrogen transport are necessary to truly answer the postulates of this section. These questions should be investigated in future studies.

Laves Phase Evolution

The variation of Laves phase across the cross-section was tested in order to determine if other factors may be at play with Laves phase precipitation in addition to temperature. The main considerations would be the hydrogen gradient and oxygen diffusion. As stated earlier, the hydrogen at interstitial sites encourages oxygen to diffuse into the interconnect material, reacting with the stainless steel alloy and forming oxides harmful for interconnect operation (29). If the formation of Laves phase precipitates is enhanced by hydrogen presence, the amount of allowed hydrogen transport may increase with exposure time.

Single Atmosphere Laves Phase Evolution

The percent surface area of the Laves phase precipitates was evaluated at specific locations on the sample cross sections [Figure 4.4.1]. This was done to determine if any gradient effects were influencing the precipitation of Laves phase nodules. Inclusion of the 95% confidence intervals shows that the difference between Laves phase precipitations at these locations is not statistically significant nor is the difference between test time intervals [Figure 4.4.2]. This holds true for all Laves phase precipitation analyses done per ImageJ. For ease of reading, the 95% confidence interval is left off the plots with the exception of this instance yet is understood to be the case throughout the analyses.

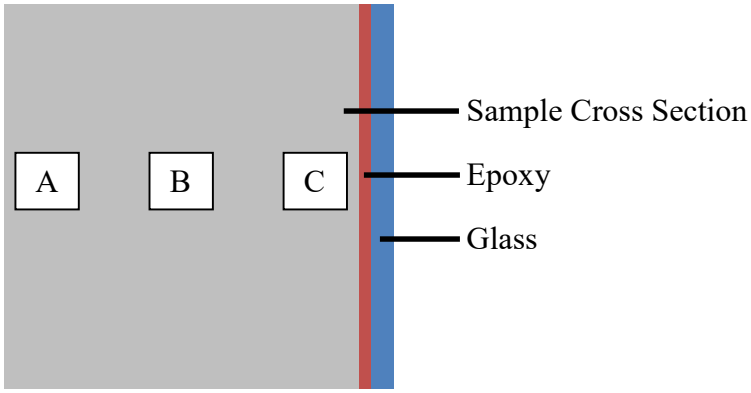

Figure 4.4.1: Location of measurements for evaluation of Laves phase precipitation where A) corresponds to Edge 1 (Hydrogen-side in DA), B) is the Center of the sample, and C) is Edge 2 (Oxygen-side in DA).

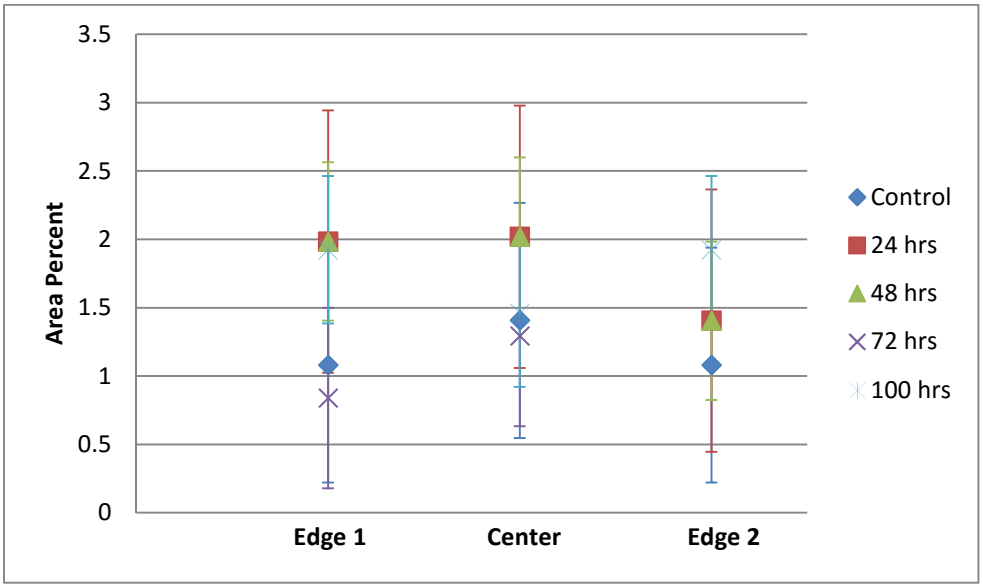

Figure 4.4.2: Laves phase area percent through cross-section of 1.2mm thick samples exposed to single atmosphere over different time intervals shown with 95% confidence intervals.

The 0.5mm thick samples exposed to single atmosphere at 800°C saw little variation in area percent of Laves phase precipitation from the sample edges to the center

of the sample. The greatest difference was with the samples exposed for100 hours to SA where a difference of 1.8 percent at the edge to 2.2 percent at the center was observed. The average area percent of Laves phase precipitation for each of the 0.5mm SA samples at various times falls between 1.4 and 2.5 area percent. Upon applying the 95 percent confidence interval, this discrepancy, despite appearing sizeable, is not statistically significant, suggesting that no trend exists in the Laves phase precipitation across the surface area in SA exposure. Rather, difference may be seen at specific locations independent of relative edge position. This supports the hypothesis that Laves phase precipitation in AISI 441 is driven by temperature and not the environment it is subjected to, corroborating studies that were also performed in a single atmosphere environment.

The 1.2 mm as-received samples contained much higher area percent values of Laves phase precipitation than the 0.5 mm as-received samples, starting at an area percent very similar to the post-experiment samples [Figure 4.4.3]. Once again, this points to material characteristics driven by the manufacturing process. The greatest variation of Laves phase precipitation in a 1.2 mm SA sample is seen in the 24 hour exposure test. In this case, a difference of 0.6 area percent is seen between the edge and center at 1.4 and 2.0 area percent, respectively. The average area percent of Laves phase precipitation for each of the 1.2 mm SA samples falls between 0.8 and 2.0 area percent, a smaller window than the 0.5 mm SA samples. These values do not trend with time or location on sample cross-section.

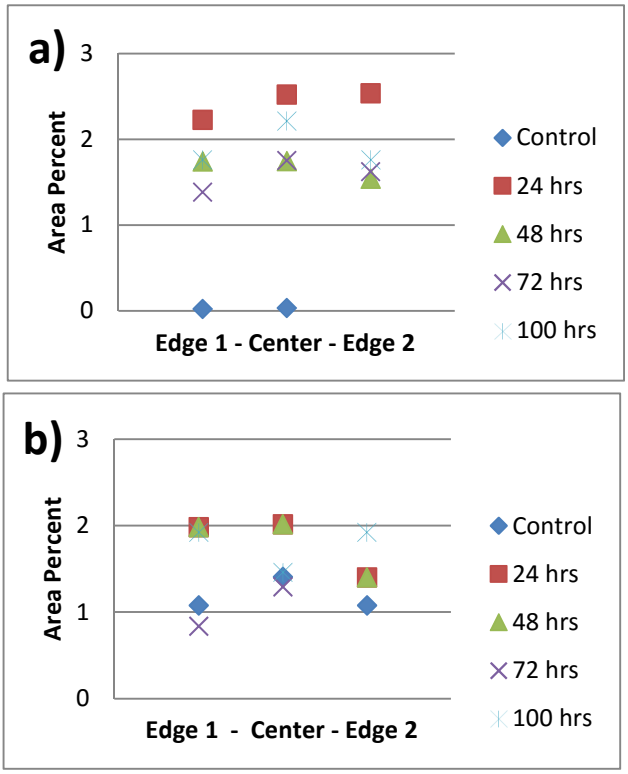

Figure 4.4.3: Laves phase area percent through cross-section of a) 0.5 and b) 1.2mm thick samples exposed to single atmosphere over different time intervals.

Dual Atmosphere Laves Phase Evolution

This section presents the effects of moist DA environments on Laves phase precipitation with pure hydrogen; the dry and partial pressure cases will be presented in Comparison. The 0.5 mm thick samples exposed to dual atmosphere at 800°C saw the greatest variation in Laves phase precipitation through the cross-section in the samples exposed for 24 hours. The difference is 0.8 area percent with 1.0 and 1.8 at the edge and center, respectively. The average area percent of Laves phase precipitation for each of the 0.5mm DA samples falls between 1.0 and 2.0 area percent.

The 1.2 mm thick samples exposed to dual atmosphere at 800°C saw the greatest variation in Laves phase precipitate through the cross-section in the samples exposed for 100 hours. The difference is 0.6 area percent with 1.6 and 2.2 percent at the edge and center, respectively. The average area percent of Laves phase precipitation for all 0.5mm DA samples falls between 1.33 and 2.34 area percent. Neither of these samples showed influence on Laves phase precipitation due to time or chemical gradients.

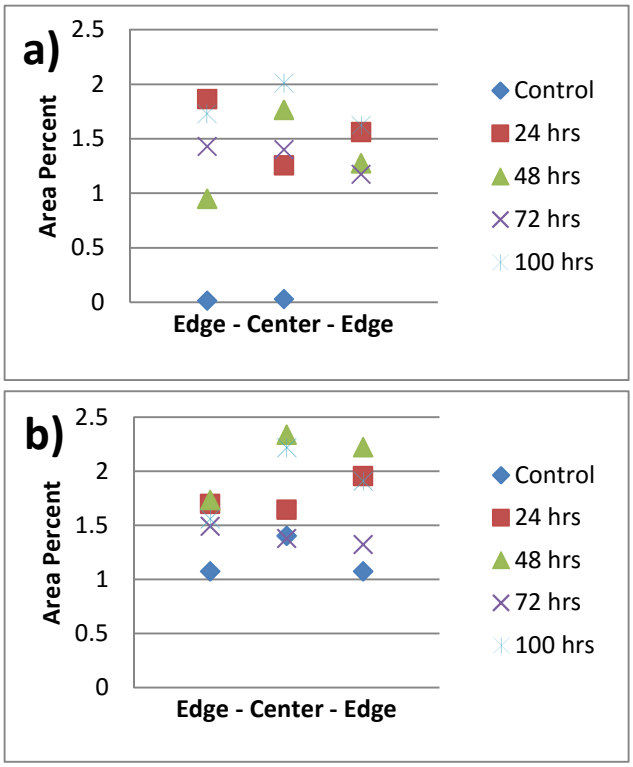

Figure 4.4.4: Laves phase area percent through cross-section of a) 0.5 and b) 1.2mm thick samples exposed to dual atmosphere over different time intervals.

Progression of Laves
Phase Density Over Time

When the 0.5 and 1.2 mm samples after SA and DA tests are compared with regards to time, the average area percent of Laves phase precipitates appears to be

constant over the given time interval [Figure 4.4.5]. Other studies have characterized the evolution of Laves phase formation over the time frame of minutes, seeing even the slowest formation saturation occurring at just over 1000 minutes: just over 16 hours (32). These tests were performed in single atmosphere furnaces between temperatures of 600 and 850°C. To view the effects that different atmospheres may have on the precipitation of these phases, future studies should look into testing at this smaller time frame.

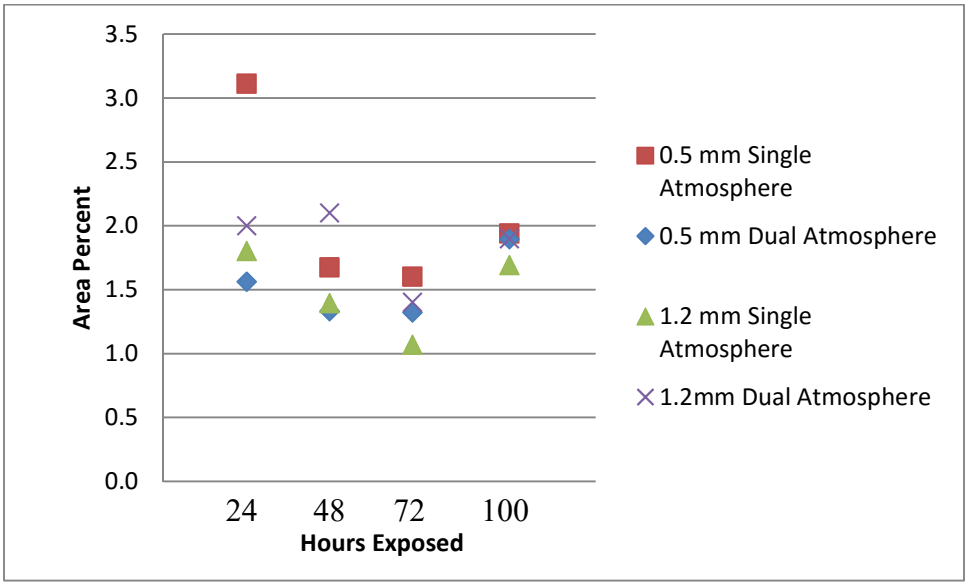

Figure 4.4.5: Average Laves phase area percent of 0.5mm and 1.2mm thick samples exposed to single and dual atmospheres at specific time intervals.

Comparison of Laves Phase
Evolution across Environment Types

Comparison of the single and dual atmosphere cases yields no trend in the development of the Laves phase precipitate over time throughout the cross-section. All averages fall between 1.0 and 2.2 area percent with the exception of the single

atmosphere 0.5mm sample at 100 hours [Figure 4.4.6]. Comparison of this selection of data to the previous cross-section data shows these data points to fall within the 95% confidence interval for Laves phase precipitation. The vacuum test over 100 hours shows the area percent of Laves phase precipitation of the indicated regions to very closely follow the area percent of the atmospheric tests, once again suggesting that the Laves phase precipitation reaches saturation due to temperature constraints and not environmental. In shorter time frame tests, different information may be gleaned; however, difficulty exists in setting up the various atmospheres within the time constraints.

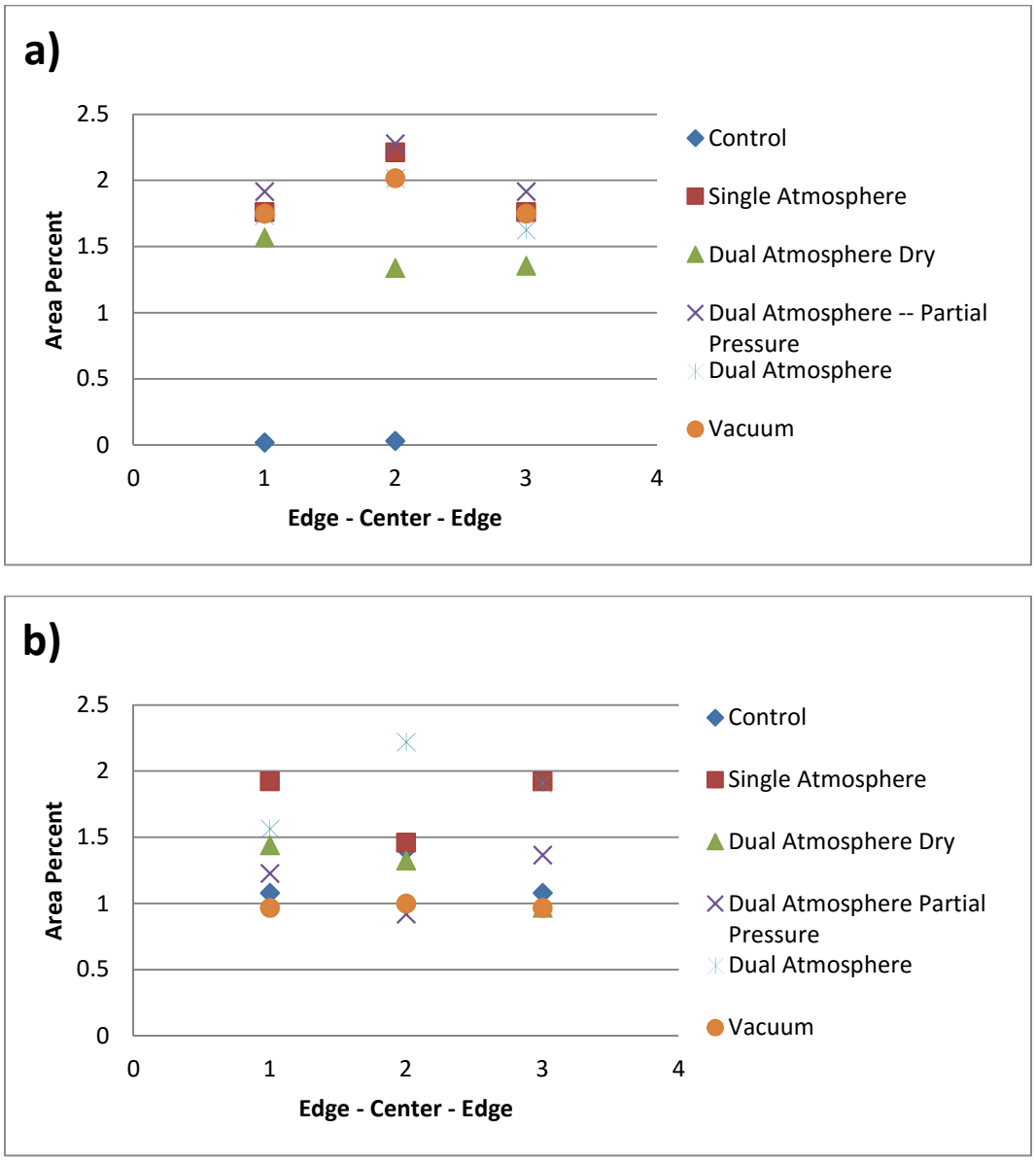

Figure 4.4.6: Laves phase area percent through cross-section of a) 0.5 and b) 1.2mm thick samples exposed to various atmospheres for 100 hours.

When placed side-by-side, the average area percent of precipitation appears to be consistently lower for the 1.2 mm samples after each of the atmospheric tests [Figure 4.4.7]. The as-received 0.5mm sample has almost no Laves phase precipitation throughout the microstructure as previously discussed. The single, dual, and dry dual atmosphere cases see very similar levels of precipitation, supporting the idea of thermally driven precipitation. The 5% partial pressure and vacuum tests show a large difference in area percent of Laves phase, but by applying the 95% confidence interval, this is seen to be the result of expected variation [Figure 4.4.7].

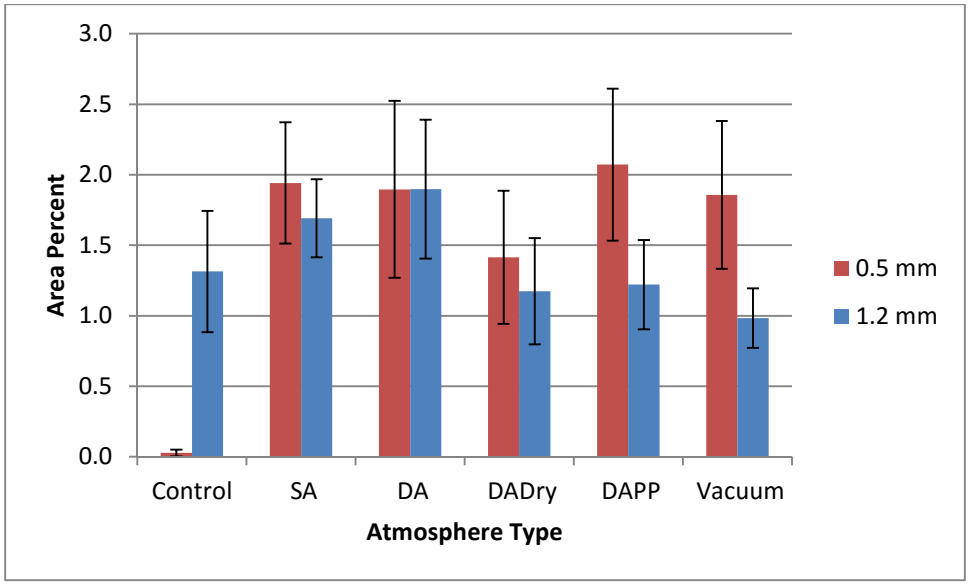

Figure 4.4.7: Average Laves phase area percent of 0.5mm and 1.2mm thick samples exposed to various atmospheres for 100 hours.

CHAPTER FIVE

CONCLUSION

Summary of Study

The precipitation of Laves phase nodules throughout the microstructure of ferritic stainless steel 441 was widely unknown in the modern application of AISI 441 as a SOFC interconnect material. Laves phase materials are under research to store hydrogen by retaining hydrogen atoms at interstitial sites. The ability to store hydrogen suggests that the Laves phase may be conducive to the flow of hydrogen through the cross-section of the material when subjected to a hydrogen gradient.

The presence of Laves phases also offers more opportunities and locations for hydrogen storage which may increase attraction on the oxygen ions into the oxide scale and metal surface, augmenting the rate of iron cation diffusion. This would, consequently, increase the rate of the oxidation reaction, leading to the observed accelerated and anomalous oxide growth. However, little is known regarding the effects of various atmospheres on the precipitation of the Laves phase nodules, spurring this study.

Initial research suggested that the precipitation may have been influenced by the type of atmosphere. Comparison of five different atmospheres – single, dual, dry dual, partial pressure dual, and vacuum – showed little variation in the area percent of precipitate seen in the electron microscope images. Furthermore, there is no statistical evidence supporting the hypothesis that atmospheric conditions affect the precipitation of

Laves phase nodules. Additionally, the uniformity of the intermetallic phase distribution from the hydrogen-side to the air-side of the sample suggests the observed precipitation is driven by temperature and not significantly affected by the hydrogen gradient. Other studies performed in single atmosphere exposure support these ideas (43).

One study characterized the formation of Laves phase precipitates due to single atmosphere isothermal testing on the time frame of minutes, with the slowest saturation occurring at just over 1000 minutes, or 16 hours (32). Since the shortest test performed for this paper's study was at 24 hours, the defining time frame for the formation of Laves phase precipitates was missed. It should also be noted that to develop from this study, as-received samples without Laves phase precipitates are necessary – a condition that the 1.2 mm thick samples did not meet.

Elemental line scans readily detect the elemental presence expected from the different oxide scales of the samples over time, corroborating previous studies on the oxide evolution in various environments. However, the exact effects of grain sizes and thicknesses on oxide development cannot be gauged from this study due to too many variables amongst samples. With regards to grain size, the 0.5 mm sample had larger grains and developed the oxide layer faster than the 1.2 mm sample. However, this could as easily be attributed to the thickness of the sample; the thinner sample allowed better hydrogen flow, increasing oxidation. Given the lack of clear data on the effects of grain sizes and sample thicknesses, this study is inconclusive in this regard.

The links between atmospheric exposure, grain size, sample thickness, Laves phase precipitation, and oxide growth has not yet been established; however, the baseline

for follow-up studies has been created through this research endeavor. Although it will truly be a difficult task to isolate variables such as Laves phase precipitation from temperature, the trends throughout this study indicate much may be gained from further pursuing this research.

Future Work

Future work will build upon the two-faceted foundation that this thesis has created. First, the refinement of processes to identify and quantify the amount of Laves phase precipitation contained within the samples. Second, the effects of these Laves phase nodules on the transportation of hydrogen through the stainless steel AISI 441 will be investigated.

Further detection of Laves phase precipitates at MSU requires a pure sample of Fe_2Nb for comparison using the XRD. By calibrating the XRD with the pure Laves phase, the percent content of Laves phase in the AISI 441 samples could be better calculated than the ImageJ technique used in this study. The AISI 441 samples would have to be ground to a powder after environmental testing, but would provide very clear, consistent results based on the chemical composition of the dust and not subject to the geometric differences of the surfaces. This testing should take place over a reduced time frame not exceeding 20 hours in order to characterize the formation time of the Laves phase under different environmental constraints. The starting samples should also contain no or little Laves phase at the start of testing.

To investigate the flow of hydrogen, gas chromatography may be used at MSU through Hugo Schmidt's lab. However, a new system needs to be built to facilitate this system. Several approaches may be taken with this, but the most consistent data will be obtained by mimicking the current system set-up with slight alterations made to allow for gas measurements to be made. This enables the sample to be held in a vertical tubular furnace with the same sealing system that is currently used with the dual atmosphere test apparatus.

The test procedure using gas chromatography has been considered but unable to be followed up on due to time and equipment restrictions. The evolution of hydrogen transport throughout heating up and dwell segments could be investigated by using a moist argon-hydrogen mixture (5 H_2: 95 Ar at ~3 vol. % H_2O). The back side would be flushed with moist pure argon in order to provide a hydrogen gradient through the AISI 441 cross-section. The flushed gas would then be analyzed via gas chromatography to determine if any difference in hydrogen concentration could be detected in the gas.

Further work must also be done investigating the effects of grain size and sample thickness on the formation of the detrimental oxide layers. Isolating these two characteristics of the material will prove difficult but allow a great deal of insight in how manufacturing techniques may improve the properties of ferritic stainless steel alloys for use in solid oxide fuel cell systems.

REFERENCES

1. *Lowering the Temperature of Solid Oxide Fuel Cells.* **Wachsman, E.D. and K.T. Lee.** s.l. : Science, 2011, Vol. 334.

2. *Direct Operation of IP-Solid Oxide Fuel Cell with Hydrogen and Methane Fuel Mixtures under Current Load Cycle Operating Condition.* **Almutairi, G. et al.** 2, Birmingham, UK : Fuel Cells, 2013, Vol. 14.

3. *Mathematical Modelling of Proton-Conduction Solid Oxide Fuel Cells and Comparison with Oxygen-Ion-Conducting Couterpart.* **Ni, M. et al.** 2006, Fuel Cells, pp. 269-278.

4. **Irvine, John T.S. and Paul Connor.***Solid Oxide Fuel Cells: Facts and Figures: Past, Present and Future Perspectives for SOFC Technologies.* London : Springer, 2013.

5. *Development of interconnect materials for solid oxide fuel cells.* **Zhu, W.Z. and S.C. Deevi.** 1-2, s.l. : Materials Science and Engineering: A, 2003, Vol. 348.

6. **EG&G Technical Service, Inc.***Fuel Cell Handbook (Seventh Edition).* Morgantown : U.S. Department of Energy, 2004. ISBN 978-0899344287.

7. *An overview of fuel cell technology: Fundamentals and applications.* **Sharaf, O.Z. and M.F. Orhan.** Sharjah, UAE : s.n., 2014, Renewable and Sustainable Energy Reviews, Vol. 32, pp. 810-853.

8. *High-Temperature, Dual-Atmosphere Corrosion on Solif Oxide Fuel Cell Interconnects.* **Gannon, P. and R. Amendola.** 12, s.l. : Journal of the Minerals, Metals, and Materials Society, 2012, Vol. 64.

9. *Stability of solid oxide fuel cell components.* **Baldwal, S.P.S.** s.l. : Solid State Ionics, 2001, Vol. 143.

10. *Interaction between chromia forming alloy interconnects and air electrode of solid oxide fuel cells.* **Baldwal, S.P.S. et al.** 1997, Solid State Ionics, p. 297.

11. *Advances in solid oxide fuel cell technology.* **Singal, S.C.** 2000, Solid State Ionics, p. 305.

12. *Materials for IT-SOFC stacks: 35 years R&D: the inevitability of gradualness.* **Steele, B.C.H.** s.l. : Solid State Ionics, 2000, Vol. 134.

13. *Solid oxide fuel cells and regenerated gas turbines hybrid systems: a feasible solution for future ultra high efficiency power plants.* **Lunghi, P. and S. Ubertini.** Tsukuba,

Ibaraki, Japan : Proceedings of the Seventh International Symposium on Solid Oxide Fuel Cells (SOFC-VII), 2001.

14. **Minh, N.Q. and T. Takahashi.***Science and Technology of Ceramic Fuel Cells.* Amsterdam : Elsevier Science B.V., 1995.

15. *Materials for electrochemical energy conversion and storage systems.* **Steele, B.C.H.** 1993, Ceramics International, pp. 269-277.

16. *Recent Developments in Solid Oxide Fuel Cell Materials.* **Yokokawa, H. et al.** 2, Tsukuba, Ibaraki, Japan : Fuel Cells, 2001, Vol. 1.

17. *Coated stainless steel 441 as interconnect materil for solid oxide fuel cells: oxidation performance and chromium evaporation.* **Grolig, J.G. et al.** 248, s.l. : Journal of Power Sources, 2014.

18. *Characterization of iron-based alloy interconnects for reduced temperature solid oxide fuel cells.* **Huang, K.** 129, s.l. : Solid State Ionics, 2000.

19. *Life prediction of coated and uncoated metallic interconnect for solid oxide fuel cell applications.* **Liu, W.N. et al.** 189, s.l. : Journal of Power Sources, 2009.

20. *Severe dual atmosphere effect at 600C for stainless steel 441.* **Alnegren, P. et al.** 301, Gothenburg, Sweden : Journal of Power Sources, 2016.

21. *Metallic interconnects for solid oxide fuel cells.* **Fergus, J.W.** 397, s.l. : Materials Science & Engineering, 2005, Vol. A.

22. **Dulieu, D. et al.** Oberrohrdorf, Switzerland : The Third European SOFC Forum, European Fuel Cell Forum, 1998.

23. *Oxidation of Alloys 430 and 441 in SOFC Dual Atmospheres: Effects of Flow Rate and Humidity.* **Zhao, Y. and J.W. Fergus.** 3, s.l. : Journal of the Electrochemical Society, 2012, Vol. 159.

24. *Oxidation behavior of stainless steel 430 and 441 at 800°C in single (air/air) and dual (air/hydrogen) exposures.* **Rufner, J. et al.** 4, s.l. : International Journal of Hydrogen Energy, 2008, Vol. 33.

25. *Oxidation Behavior of Ferritic Stainless Steels under SOFC Interconnect Exposure Conditions.* **Yang, Z.G. et al.** 12, s.l. : Journal of the Electrochemical Society, 2004, Vol. 151.

26. *Screen-printed (La,Sr)CrO3 coatings on ferritic stainless steel interconnects for solid oxide fuel cells using nanopowders prepared by means of ultrasonic spray pyrolysis.* **Brylewski, Tomasz et al.** 2012, Journal of Power Sources, pp. 86-95.

27. *Cu- and Ni-doped Mn1.5Co1.5O4 spinel coatings on metallic interconnects for solid oxide fuel cells.* **Park, Beom-Kyeong et al.** 2013, International Journal of Hydrogen Energy, pp. 12043-12050.

28. *Physical properties of hematite α-FE2O3 thin films: application to photoelectrochemical solar cells.* **Shinde, s. et al.** 1, Kolhapur, India : Journal of Semiconductors, 2011, Vol. 32.

29. *The Mechanism of teh High-Temperature Oxidation of Iron-Chromium Alloys in Water Vapor.* **Fujii, C.T. et al.** 1964, The Electrochemical Society, pp. 1215-1221.

30. *High Temperature Oxidation Behaviour of Ferritic Stainless Steel SUS 430 in Humid Air.* **Cheng, X. et al.** 2015, Metals and Materials International, pp. 251-259.

31. **Ashbey, M. et al.***Materials: Engineering, Science, Processing, and Design.* Burlington, MA, USA : Butterworth-Heinemann, 2010.

32. *Laves phase precipitation and its transformation kinetics in ferritic stainless steel type AISI 441.* **Sello, M.P. and W.E. Stumpf.** A528, s.l. : Materials Science and Engineering, 2011.

33. *Laves phase embrittlement of the ferritic stainless steel type AISI 441.* **Sello, M.P. and W.E. Stumpf.** A527, s.l. : Materials Science and Engineering, 2010.

34. **Yakoubi, A. et al.***Structural and electronic properties of the Laves Phase Based on Rare Earth Type BaM2 (M = Rh, Pd, Pt).* Sidi Bel-Abbes, Algeria : Elsevier, 2012.

35. *Hydrogen Absorption/Desorption Properties in the TiCrV Based Alloys.* **Martinez, A and D.S. dos Santos.** 2012, Materials Research, pp. 809-812.

36. *Laves phase hydrogen storage alloys for super-high-pressure metal hydride hydrogen compressors.* **Xiumei, Guo et al.** 3, Beijing : Rare Metals, 2010, Vol. 30.

37. *A correlation between the interstital hole sizes in intermaetallic compounds and the thermodynamic properties of the hydrides formed from those compounds.* **Lundin, C.E. et al.** 1, s.l. : Journal of the Less Common Metals, 1977, Vol. 56.

38. *Dual-Environment Effects on the Oxidation of Metallic Interconnects.* **Holcomb, G.R. et al.** 4, s.l. : Journal of Materials Engineering and Performance, 2006, Vol. 15.

39. **Gill, Zachary Edward.***A Fundamental Study of Hot Corrosion and Interdiffusion of Chromium, Aluminum, and Silicon Coatings on Nickel 201 Substrate.* Bozeman, Montana, United States of America : s.n., May 5, 2014.

40. **Aw, Lik Ming.***DEVELOPMENT OF BINARY AND TERNARY CHROMIUM, ALUMINUM, CARBON THIN FILM COATINGS FOR HOT CORROSION PREVENTION.* Bozeman, Montana, United States of America : s.n., January 2015.

41. **Imaging and Chemical Analysis Laboratory.** Scanning Electron Microscope: JEOL JSM-6100. *Montana State University.* [Online] 2011. http://www.physics.montana.edu/ical/instrumentation/sem.asp.

42. **ASTM International.***ASTM E112-113: Standard Test Methods for Determining Average Grain Size.* West Conshohocken, PA : s.n., 2013.

43. *Investigation of iron-chromium-niobium-titanium ferritic stainless steel for solid oxide fuel cell interconnect applications.* **Yang, Z. et al.** 2, s.l. : Journal of Power Sources, 2008, Vol. 183.